A Prognostic Cloud Water Parameterization for Global Climate Models

ANTHONY D. DEL GENIO

NASA Goddard Institute for Space Studies, New York, New York

MAO-SUNG YAO, WILLIAM KOVARI, AND KENNETH K.-W. LO

Science Systems and Applications, Inc., Institute for Space Studies, New York, New York

(Manuscript received 25 January 1995, in final form 3 July 1995)

ABSTRACT

An efficient new prognostic cloud water parameterization designed for use in global climate models is described. The scheme allows for life cycle effects in stratiform clouds and permits cloud optical properties to be determined interactively. The parameterization contains representations of all important microphysical processes, including autoconversion, accretion, Bergeron–Findeisen diffusional growth, and cloud/rain water evaporation. Small-scale dynamical processes, including detrainment of convective condensate, cloud-top entrainment instability, and stability-dependent cloud physical thickness variations, are also taken into account. Cloud optical thickness is calculated from the predicted liquid/ice water path and a variable droplet effective radius estimated by assuming constant droplet number concentration. Microphysical and radiative properties are assumed to be different for liquid and ice clouds, and for liquid clouds over land and ocean.

The parameterization is validated in several simulations using the Goddard Institute for Space Studies (GISS) general circulation model (GCM). Comparisons are made with a variety of datasets, including ERBE radiative fluxes and cloud forcing, ISCCP and surface-observed cloud properties, SSM/I liquid water path, and SAGE II thin cirrus cover. Validation is judged on the basis of the model's depiction of both the mean state; diurnal, seasonal, and interannual variability; and the temperature dependence of cloud properties. Relative to the diagnostic cloud scheme used in the previous GISS GCM, the prognostic parameterization strengthens the model's hydrologic cycle and general circulation, both directly and indirectly (via increased cumulus heating). Sea surface temperature (SST) perturbation experiments produce low climate sensitivity and slightly negative cloud feedback for globally uniform SST changes, but high sensitivity and positive cloud feedback when tropical Pacific SST gradients weaken with warming. Changes in the extent and optical thickness of tropical cumulus anvils appear to be the primary factor determining the sensitivity. This suggests that correct simulations of upward transport of convective condensate and of Walker circulation changes are of the highest priority for a realistic estimate of cloud feedback in actual greenhouse gas increase scenarios.

1. Introduction

Almost all climate GCMs agree that total cloud cover should decrease while cloud height increases in response to a greenhouse gas–induced warming (Del Genio 1993). This agreement is surprising, since there is no fundamental basis for predicting the sign of cloud cover changes. Despite this consensus, GCM estimates of cloud feedback range from strongly positive to weakly negative. Much of the disagreement can be traced to the models' differing representations of cloud radiative properties and the resulting optical thickness feedback. There are essentially three different approaches to the parameterization of cloud optical properties in GCMs:

1) *Implicit:* Many GCMs prescribe cloud optical thickness (or shortwave albedo and longwave emissivity) as a fixed function of altitude. Since cloud height increases with warming, this induces an implicit cloud optics feedback. The feedback is typically positive because optical thickness decreases with height in most models and the albedo effect dominates the greenhouse effect of clouds globally. But negative feedback examples also exist, for example, in models that prescribe extensive, thick cumulus anvils (cf. Cess et al. 1990).

2) *Temperature-dependent:* Several GCMs diagnose optical thickness as a function of temperature, based on the instantaneous condensation needed to eliminate supersaturation or the adiabatic liquid water content of a lifted cloud (Betts and Harshvardhan 1987). This is a flawed approach: Such schemes parameterize the source, but none of the sinks, of cloud water and imply constant cloud physical thickness. Consequently, albedo systematically increases with warming, and as a result these models tend to be biased toward negative cloud optics feedback.

Corresponding author address: Dr. Anthony D. Del Genio, NASA Goddard Institute for Space Studies, 2880 Broadway, New York, NY 10025.
E-mail: pdadd@nasagiss.giss.nasa.gov

3) *Prognostic:* The most recent trend in GCMs is to carry cloud water content as a prognostic variable, thus permitting storage of cloud water and life cycle effects as well as interactive optical properties (Sundqvist 1978; Roeckner et al. 1987; Smith 1990; LeTreut and Li 1991; Tiedtke 1993). This approach is in principle the most physically realistic. But it requires the parameterization of complex microphysical, dynamic, and radiative processes, thus introducing a number of degrees of freedom absent from the simpler approaches. Not surprisingly, GCMs with prognostic schemes can produce either positive, negative, or nearly neutral cloud feedback.

Because of the wide variety of processes that must be accounted for and the requirement for simple representations of these processes to permit long model integrations, prognostic cloud parameterizations cannot yet be considered superior to the simpler approaches in their predictive ability. However, implicit and temperature-dependent approaches have very limited potential to either improve in response to advances in understanding or to shed light on the physics of cloud feedback. Models with prognostic schemes can instead be regarded as laboratories that enable us to assess which cloud processes are most important to changing climate. Ideally, then, such models can not only exploit new information but can also guide the strategy for future observations and theoretical studies. Note that the advantage of prognostic schemes is not the new prognostic variable per se, but rather the attempt to include physically reasonable representations of processes. In some cases diagnostic process formulations may be a useful approach to parameterization (cf. Heymsfield and Donner 1990), and these have much in common with prognostic schemes. Even in prognostic parameterizations, certain aspects are often diagnosed (precipitation, cloud cover, particle size).

The performance of prognostic cloud parameterizations is limited by 1) poorly understood cloud processes (e.g., cloud-top entrainment instability); 2) inadequate observations of cloud properties (e.g., ice water content); 3) cloud physics that is computationally not feasible to simulate in GCMs (e.g., evolution of drop size distributions); 4) physics that is understood on the cloud scale but not on the GCM grid scale (e.g., relationship of cloud cover to relative humidity); 5) deficiencies in other parts of the GCM (e.g., surface and boundary layer fluxes and large-scale dynamical transports). Consequently, all parameterizations must contain arbitrary tuning parameters. These can give a parameterization the appearance of performing well while actually obscuring the issue of whether it contains the appropriate physics for its intended applications. To avoid this trap, we adopt the following approach to parameterization:

1) Tuning parameters must not be arbitrary functions of latitude, altitude, etc. Ideally they should be functions of a model-predicted quantity based on known physics or at least empirical evidence, but in the absence of either, tuning parameters must be globally uniform constants. This reduces the possibility of misleading apparent validation of the scheme via a well-chosen comparison with a particular dataset. In the long run, climate model development and observing program design are better served by highlighting model-data discrepancies than by artificial agreement based on arbitrary assumptions.

2) Validation of the scheme must be performed against multiple datasets. For example, accurate simulation of top-of-the-atmosphere (TOA) radiative fluxes is a necessary but not sufficient condition for validation. Since the fluxes are the composite effect of spatially and temporally varying cloud cover, cloud optical properties, water vapor, etc., validation of each individual quantity must be conducted to ensure that accurate radiative fluxes are not simply the result of compensating errors in several parameters.

3) For climate models, which predict change, much of the validation must be done against variability of the current climate, not just the mean state. This is the model analog to the issue of accuracy versus precision for scientific instruments: the accuracy of the absolute value of an observed (simulated) parameter is often worse, but less important, than our ability to detect (predict) changes to high precision. Of course variability may depend on the mean state, but if variability is directly validated against data, errors in sensitivity caused by errors in the mean state will be evident. This is not to say that the mean state is unimportant; errors in the mean state may cause climate drift in a coupled atmosphere–ocean GCM. Thus, both mean state and variability must be examined.

With these considerations in mind, in this paper we describe a new prognostic cloud water budget parameterization that has been implemented in the GISS GCM. Details of the scheme are presented in section 2. Section 3 describes the model's mean state, spatial variability, and the effect of the cloud scheme on the general circulation. Section 4 documents its simulated diurnal, seasonal, and interannual variability. Section 5 examines the GCM's simulation of the temperature dependence of cloud properties and its sensitivity to prescribed SST perturbations. In section 6 we discuss the implications of our work for future observations and for understanding climate sensitivity to realistic climate forcings.

2. Model description

The baseline GISS GCM, Model II, is described in Hansen et al. (1983). The new cloud parameterization was implemented in an updated version of the GCM, run at 4° × 5° horizontal resolution with nine vertical levels. Aside from the prognostic cloud scheme, the

updated GCM differs from Model II in that it contains improved parameterizations of moist convection (Del Genio and Yao 1993), the planetary boundary layer (Hartke and Rind 1995), and ground hydrology (Rosenzweig and Abramopoulos 1995), and uses the quadratic upstream scheme for advection of heat and moisture (similar to that described in Prather 1986). The GCM was run on an IBM RISC6000 580 workstation, requiring about 8.3 CPU minutes per simulated day; 10%–15% of the CPU time is used for parameterized moist processes (convection + stratiform clouds). Validation and sensitivity assessment are based on three model runs: 1) a 6-yr simulation with climatological SSTs, the results being averaged over the final 5 years; 2) a 10-yr AMIP run with actual SSTs for the period 1979–1988; 3) several 1-yr perpetual July runs with prescribed SST perturbations, the results being averaged over the last 7 months. Shorter sensitivity tests have also been conducted to isolate impacts of certain aspects of the model physics. Details of the prognostic cloud water budget parameterization are described below.

a. Cloud water formation and evolution

To parameterize stratiform cloud generation, we follow the approach of Sundqvist et al. (1989). We divide the gridbox into a cloudy part (with fractional cloudiness b and relative humidity $U_s = 1$) and a clear part (with relative humidity U_0). The gridbox mean relative humidity is then

$$U = bU_s + (1 - b)U_0. \tag{1}$$

As in Sundqvist (1978), net latent heating of the gridbox due to stratiform cloud phase changes (Q) equals the condensation heating in the cloudy part (Q_c) minus the evaporation of cloud water (E_c) and rainwater (E_r) in the clear part; that is,

$$Q = bQ_c - (1 - b)(E_c + E_r). \tag{2}$$

The continuity equation for the dimensionless cloud water content m can then be written

$$\frac{\partial m}{\partial t} = A(m) + b\frac{Q_c}{L} - (1 - b)\frac{E_c}{L} - P + S_s$$

$$= A(m) + \frac{Q}{L} + (1 - b)\frac{E_r}{L} - P + S_s, \tag{3}$$

where t is time, $A(m)$ is the large-scale advection of cloud water, P is the conversion rate of cloud water to precipitation, L is the latent heat of condensation/deposition, and $S_s = S_d + S_e$ is the subgrid-scale dynamical source/sink of cloud water due to convective condensate detrainment (S_d) and cloud-top entrainment instability (S_e). The water vapor continuity equation thus includes a sink term $-Q/L$, and the thermodynamic energy equation a source term proportional to Q/c_p, determined by (2) rather than by the phase change required to eliminate supersaturation that is characteristic of diagnostic schemes.

Sundqvist shows that stratiform latent heating can be expressed in terms of the gridbox mean relative humidity tendency as

$$Q = \frac{M - Lq_s\dfrac{\partial U}{\partial t}}{1 + \dfrac{U\epsilon L^2 q_s}{Rc_pT^2}}, \tag{4}$$

where M is the convergence of available latent heat into the gridbox (including the effects of temperature and pressure changes), q_s is the saturation specific humidity, ϵ is the ratio of the molecular weights of water vapor and dry air, R is the gas constant for dry air, c_p is the specific heat of dry air, and T is temperature. If we assume that the total source of water vapor from dynamic convergence and evaporation $M + (1 - b)(E_c + E_r)$ is divided into a part bM that condenses into the already cloudy fraction of a gridbox, and another part $(1 - b)(M + E_c + E_r)$ that increases the cloud cover and the relative humidity of the clear fraction, then it can be shown that (Sundqvist et al. 1989)

$$\frac{\partial U}{\partial t} = \frac{2(1 - b)^2(U_s - U_{00})(M + E_c + E_r)}{L[2q_s(1 - b)(U_s - U_{00}) + m/b]} \tag{5}$$

(U_{00} is defined below). Equation (5) is used to calculate the heating term (4), which is then used to predict the tendency of cloud water (3) at each physics time step (1 h).

b. Cloud cover and morphology

We specify a threshold relative humidity U_{00} below which stratiform cloud formation does not occur, and we assume that the relative humidity of the clear fraction increases as the cloud fraction increases (Sundqvist et al. 1989) according to

$$U_0 = U_{00} + b(U_s - U_{00}). \tag{6}$$

Here U, U_0, and U_{00} are ratios of vapor pressures to saturation values, but there is uncertainty in how to appropriately define saturation vapor pressure at cold temperatures due to the complexity of the ice phase initiation process. As temperature decreases, the relative contributions of heterogeneous and homogeneous freezing (which require liquid water saturation) and deposition (which requires only ice saturation) systematically vary. To account for this we define relative humidity with respect to the saturated vapor pressure over liquid water (e_{sw}) for temperatures above −35°C, and with respect to the mixed phase pseudoadiabatic process proposed by Sassen and Dodd (1989) for lower temperatures:

$$e_s/e_{sw} = 5.36 \times 10^{-3}\,T(K) - 0.276. \tag{7}$$

We take $U_{00} = 0.6$ [relative to e_s as defined by Eq. (7)] for all clouds.

The cloud cover used to define U_0 in (6) is that from the previous time step. After microphysical processes change U, the stratiform cloud fraction is updated using (1) as

$$b = \frac{U - U_0}{U_s - U_0}. \quad (8)$$

Although it is plausible that clear-sky relative humidity should be positively correlated with cloud cover on climatic timescales, there is no direct observational support for the use of (6) on an instantaneous basis or for the concept of a threshold relative humidity. Recent analyses of cloudiness in the upper troposphere using GOES 6.7-μm data (Soden and Bretherton 1993), and in the lower troposphere using radiosonde data in tandem with a mesoscale model (Walcek 1994), suggest that a threshold relative humidity does not exist and that cloudiness is an almost linear function of large-scale relative humidity, with significant scatter. The GCM, despite its 60% threshold, produces some cloudiness at drier humidities because 1) the saturation reference at cold temperatures [Eq. (7)] is less than that for water saturation, and 2) convective cloud cover in the GCM is parameterized according to the fraction of layer mass rising in convection rather than as a function of relative humidity. Nonetheless, the GCM underpredicts (overpredicts) cloud cover at low (high) relative humidity. On the other hand, the parameterization (6)–(8) performs satisfactorily compared to cloud ensemble model statistics (Xu and Krueger 1991).

Other approaches to parameterization such as cloud cover based on subgrid-scale deviations of temperature and moisture are equally plausible and theoretically preferable, but the specifics are similarly unconstrained by data. The arbitrary nature of assumed subgrid-scale variations in global climate models can in fact have significant unintended impacts on cloud feedback (Miller and Del Genio 1994). Thus, at the current time there is no clear choice for the best way to predict cloud cover variations in GCMs, other than to ensure that they are statistically positively correlated with relative humidity variations. As an extreme example of the importance of uncertainties in cloud cover formulation, we performed a sensitivity test in which we set $b = 1$ whenever $U > U_{00}$. This causes large-scale condensation and precipitation, which are smaller than convective heating and precipitation in the control, to become significantly larger instead, while mean relative humidity and high cloud cover actually decline noticeably.

Although (8) is typically interpreted as the cloud cover (i.e., the horizontal area fraction covered by cloud as viewed from above), it is actually the fraction of the gridbox volume occupied by clouds. GCM vertical resolution is too coarse to resolve many clouds, for example, layered stratus and cirrus in stable environments. As a result, if clouds are assumed to fill the gridbox vertically, cloud cover is underestimated while optical thickness (τ) is overestimated. For all but the optically thinnest clouds, the net effect is an underestimate of solar reflection, since reflectance increases less than linearly with optical thickness.

We therefore distribute the cloud fraction b evenly in all three dimensions in stable situations. This allows for the possibility of cloud physical thickness less than the GCM layer thickness for the purpose of estimating optical thickness. The cloud cover (b') and cloud optical thickness (τ') used for radiation calculations are thus given by

$$b' = b^{2/3}$$
$$\tau' = b^{1/3}\tau. \quad (9)$$

In gridboxes in which moist convection has occurred, the environment is assumed to be disturbed and the clouds more vertically than horizontally developed; in such cases the original b and τ are used for radiative purposes instead. In the lowest model layer, an analogous choice is made in the presence/absence of cloud-top entrainment instability (see section 2d). This approach is at least qualitatively consistent with the observed tendency for layered stratus incidence to increase with stability (Klein and Hartmann 1993). It has a positive impact on the simulated global cloud cover and radiation balance, quantities that are biased low and high, respectively, in most GCMs.

Radiation computations in the GISS GCM are performed once per gridbox for either clear or cloudy conditions. For this purpose the box is determined to be either clear or 100% cloud-covered by comparing the fractional cloud cover determined by the cloud parameterization to a random number between 0 and 1 (Hansen et al. 1983). Fractional cloudiness in time is thus used as a proxy for subgrid-scale spatial fractional cloudiness. A single random number is chosen for the entire grid column; this is tantamount to a maximum overlap assumption. A sensitivity test using a different random number for each layer, which produces statistics more like those for random overlap instead, increases the global cloud cover by several percent and reduces solar absorption by about 2 W m^{-2} globally but affects the zonal mean by no more than 7 W m^{-2} at any latitude.

c. Cloud microphysics

Autoconversion of cloud water to precipitation should be an increasing function of the density of condensate inside the cloud. The cloud water density within the cloud is given by $\mu = m\rho/b$. Precipitation formation is then parameterized as

$$P = C_0 m\left\{1 - \exp\left[-\left(\frac{\mu}{\mu_r}\right)^4\right]\right\} + C_1 m P_r, \quad (10)$$

where μ_r is a critical cloud water content for the onset of rapid conversion, C_0 is the limiting autoconversion rate for large μ, C_1 is an efficiency factor for accretion of cloud water by precipitation, and P_r is the precipitation flux entering the layer from above. Equation (10) is similar to expressions suggested by Sundqvist et al. (1989) and Smith (1990) but with a larger exponent in the autoconversion term. This provides a sharper transition from weakly to strongly precipitating clouds but has a relatively minor effect on the simulation.

Our parameterization differs from that of previous models in three important ways:

1) We use (10) for both liquid and ice phase clouds, differentiating between the two only with different values of μ_r, because the same microphysics is just operating under different parameter settings. The UKMO GCM, for example, invokes a different representation for ice clouds that produces immediate precipitation (Smith 1990). In climate change simulations with this GCM, the resulting short lifetime of ice clouds has important effects on the predicted cloud feedback (Mitchell et al. 1989), yet observational support for systematically different lifetimes for ice and liquid clouds does not exist.

2) Precipitation formation is easier in maritime clouds than continental clouds, all other things being equal, because of the larger cloud condensation nucleus (CCN) concentration and resulting smaller droplet sizes over land (Twomey 1977). We therefore adopt different values of μ_r for liquid phase clouds over land and ocean.

3) The limiting autoconversion rate C_0 is related to the coalescence and sedimentation rates of droplets in static conditions. But clouds often form in regions of strong rising motion, which inhibits sedimentation. We ignore vertical advection of cloud water (see section 2d), and in any case climate GCMs do not resolve the scales of vertical motion relevant to sedimentation. We therefore compensate for the absence of this physics by parameterizing C_0 as a decreasing function of the large-scale vertical velocity w (the gridbox mean minus any cumulus subsidence) in regions of uplift according to

$$C_0 = \begin{cases} C_{00} 10^{-w/w_0} & (w \geq 0) \\ C_{00} & (w < 0) \end{cases} \quad (11)$$

In the current version of the model, the microphysical constants are set to the following values: $\mu_r = 0.5$ (liquid, ocean), 1.0 (liquid, land), 0.1 (ice) g m^{-3}, $C_{00} = 10^{-4}$ s^{-1}, $w_0 = 1$ cm s^{-1}, and $C_1 = 1$ m^2 kg^{-1}. The critical cloud water contents are chosen to be comparable to observed upper limits (Stephens et al. 1978; Hobbs and Rangno 1985; Heymsfield and Donner 1990), consistent with the assumption that cloud water removal by precipitation approximately balances production by condensation in the mature stage of the cloud life cycle. The limiting autoconversion rate is specified based on microphysics calculations, which indicate that stratiform clouds typically require several hours to reach the precipitating stage (Mason 1971). Here C_{00} is the same for liquid and ice; the actual autoconversion rate differs for the two phases only to the extent that μ exceeds μ_r more easily for ice than for liquid. The accretion constant is chosen arbitrarily to make accretion competitive with autoconversion only for massive precipitating cloud systems.

We use a single prediction equation for all condensate regardless of phase. We assume that all clouds in a gridbox form as liquid when the temperature $T > T_0$, where $T_0 = -4$°C over ocean and -10°C over land, based on observations compiled by Hobbs and Rangno (1985). For $T < -40$°C, all clouds form as ice. In between, the probability P_i of ice formation in a given gridbox layer is given by

$$P_i = 1 - \exp\left[-\left(\frac{T_0 - T}{15}\right)^2\right]. \quad (12)$$

The choice of phase is then made by comparing P_i to a random number. Equation (12) implies equal probability of liquid and ice formation at temperature $T_0 - 12.5$°C—that is, -16.5°C (ocean) and -22.5°C (land). Falling snow melts in the layer in which the 0°C isotherm is crossed.

After the initial decision to form liquid or ice in a given layer, mixed phase processes can change the phase if ice falls into a lower layer containing supercooled liquid water. We parameterize Bergeron–Findeisen diffusional growth of the ice phase at the expense of the liquid phase via the "seeder–feeder" process by allowing a layer with supercooled water to glaciate if sufficient ice falls into it from above. We compute the probability of glaciation as

$$P_g = \{1 - \exp[-(M_i/M_l)^2]\} \times \{1 - \exp[-(C_0 C_B \Delta t/2)^2]\}, \quad (13)$$

where M_i and M_l are the mass of ice entering the layer and the mass of supercooled liquid in the layer, respectively, and

$$C_B = 1 + \exp\left[-\left(\frac{T + 15}{10}\right)^2\right], \quad (14)$$

with T in °C. Here P_g is compared to a random number to determine whether glaciation actually occurs in a given layer and time step. Upon glaciating, the value of C_0 used in the autoconversion estimate (11) for that layer also increases by the factor C_B.

The first term in (13) is designed to limit the occurrence of the Bergeron–Findeisen process when only trace amounts of ice are falling into a supercooled region. Thus, given a multilayer cloud with ice at the top and supercooled liquid below, the cloud can gradually glaciate from the top down as ice phase mass and sedimentation increase. Such clouds can then go through a life cycle in which the ice phase is increasingly pre-

ferred as the cloud ages. The second term in (13) allows for maximum probability of Bergeron–Findeisen growth near $T = -15$°C, where the difference between the saturation vapor pressures with respect to liquid and ice is large. The frequency of occurrence of the Bergeron–Findeisen process in the GCM is displayed in Fig. 1; it is most important at midlevels in the Tropics and summer midlatitudes, and in the lower troposphere in the winter midlatitudes. Diffusional growth due to the presence of mixed phase clouds in a single layer can occur if condensate is detrained from a cumulus updraft into an anvil cloud of different phase.

The combined result of (12) and (13) is that the fractional occurrence of ice versus liquid varies with temperature as shown in Fig. 2. Supercooled liquid persists down to temperatures approaching −40°C over land, consistent with in situ observations compiled by Feigelson (1978). Over ocean, the liquid phase disappears more rapidly with decreasing T and is almost nonexistent below −30°C, consistent with SMMR retrievals (Curry et al. 1990). The behavior in Fig. 2 differs from that assumed in the UKMO GCM, in which the transition from liquid to ice occurs completely between 0°C and −15°C (Smith 1990). Cloud feedback in that GCM (Mitchell et al. 1989; Senior and Mitchell 1993) may be negatively biased as a result (Li and LeTreut 1992). It is worth noting that in the GISS GCM, negative feedbacks due to differing ice versus liquid cloud lifetimes may be minimized in any case because 1) we assume the same limiting autoconversion rate for ice and liquid in the absence of observations to the contrary, and 2) the Bergeron–Findeisen process parameterization shortens the lifetime of supercooled liquid clouds underlying ice clouds.

Evaporation of cloud water is neglected in many GCMs but is important when clear air is turbulently entrained into the cloud. This is a complex dynamical problem that defies easy parameterization. To incorporate at least the basic microphysics, we define the droplet evaporation rate as (Twomey 1977; Schlesinger and Oh 1993)

$$t_{ed}^{-1} = -\frac{1}{r}\frac{dr}{dt} = \frac{1 - U_0}{(K_1 + K_2)r^2}, \tag{15}$$

where

$$K_1 = \frac{L^2\rho_w}{kR_vT^2}, \quad K_2 = \frac{R_vT\rho_w}{De_s(T)}. \tag{16}$$

In (15) and (16), r is the droplet radius, ρ_w is the density of water, k is the thermal conductivity of air, R_v is the gas constant for water vapor, and D is the diffusivity of water vapor in air. The droplet radius is diagnosed from the cloud water content (section 2e).

The cloud water evaporation rate on the GCM grid scale (t_e^{-1}) is much less than this, because only a small fraction of the cloud mixes with clear air at any time, and droplets in the fraction that does are exposed to a

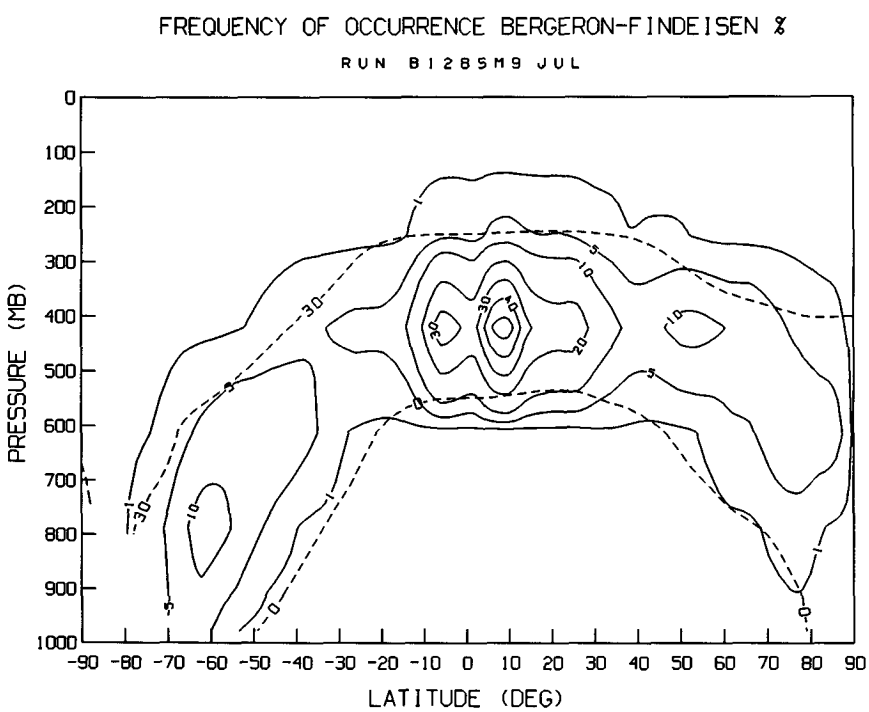

FIG. 1. Zonal mean frequency of occurrence (%) of Bergeron–Findeisen diffusional growth of ice crystals in July as simulated by the GCM. Dashed lines indicate the 0°C and −30°C isotherms.

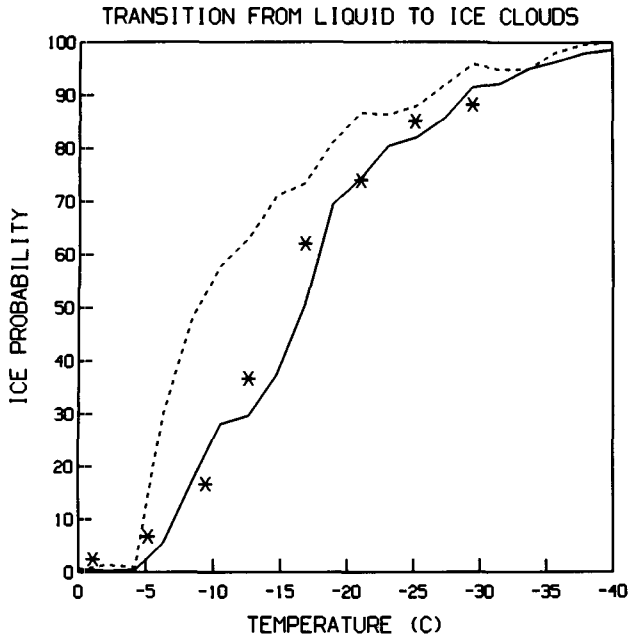

FIG. 2. Probability of condensate occurring as the ice phase (%) vs layer temperature (°C), binned at 2°C intervals, for grid points over land (solid line) and ocean (dashed line) as simulated by the GCM. Asterisks denote observations compiled by Feigelson (1978) over land.

relative humidity $U_0 < U < 1$ because of the mixing. We thus set $t_e^{-1} = \alpha t_{ed}^{-1}$, with $\alpha \ll 1$ being a free parameter that incorporates not only the dynamical uncertainties but also the complexity associated with the presence of a spectrum of droplet sizes, each with a different evaporation rate. There is little guidance as to the appropriate magnitude of α. A water budget study of upper troposphere cumulus anvils suggests that cloud water evaporation is a small contributor (Gamache and Houze 1983), but entrainment is thought to significantly dilute the properties of low-level marine stratus (Hanson, 1991). We take $\alpha = 10^{-3}$, which makes cloud evaporation an important sink for liquid clouds but generally unimportant for ice clouds because of the temperature dependence of e_s (Fig. 3). Plausibly, α might be made a function of stability instead. The cloud water evaporation rate in energy units is then estimated as

$$E_c = \alpha \frac{Lm/b}{t_{ed}} = \frac{Lm/b}{t_e}. \tag{17}$$

Rain (snow) evaporation (sublimation) affects cloud water content indirectly by changing the gridbox relative humidity. We parameterize it following Sundqvist (1978) as

$$E_r = \frac{g}{\Delta p}(U_s - U_0)LP_r, \tag{18}$$

where g is the acceleration of gravity and Δp the layer pressure thickness. Precipitation that does not evaporate falls to the ground in one physics time step (1 h), that is, there is no precipitation budget in the model. This is a good approximation for rain falling from low levels but not for ice crystals precipitating from high altitude.

d. Subgrid-scale cloud dynamical processes

We ignore advection of cloud water by the large-scale dynamics in this version of the GCM, that is, $A(m) = 0$ in (3). The justification for this is twofold: 1) cloud water contents are typically 1–2 orders of magnitude less than the water vapor content of a gridbox, so cloud water has little effect on the overall water transport; 2) the residence time of cloud water in the atmosphere (approximately $C_0^{-1} \approx 10^4$ s) is much less than that of water vapor ($10^5 - 10^6$ s). Thus, over the lifetime of a typical cloud, a wind of 50 m s^{-1} would be required to transport a substantial fraction of the cloud water even one gridbox horizontally in a model with 4° × 5° resolution. Vertical transport of cloud water is assumed to roughly offset sedimentation, which is approximately true for droplets of radius 10 μm and typical large-scale vertical velocities of several cm s^{-1}. The effect of variable vertical velocities is crudely accounted for via the parameterized dependence of C_0 on w in (11).

Several subgrid-scale dynamical processes associated with vigorous vertical motion can have noticeable effects on cloud water content and optical properties, however. In mesoscale cirrus anvils associated with deep convective clusters, for example, convective condensate is transported vertically and is partly detrained into the anvil. An analysis of the water budget of a GATE cluster suggests that a significant fraction of the anvil water is detrained from the cumulus updraft rather than produced locally by stable ascent and condensation within the anvil itself (Gamache and Houze 1983). This too is a complex dynamical problem, requiring information on cumulus updraft speeds and convective droplet size distributions. We simply assume that the water condensed at any level above the 550-mb level in deep cumulus updrafts (m_c) is added to any existing stratiform cloud water at those levels—that is, $S_d = m_c/\Delta t$ in (3), where $\Delta t = 3600$ s is the physics time step. In other words, upper troposphere convective condensate is "detrained" into a stratiform anvil and evolves according to the cloud water budget equation (3) rather than precipitating immediately, as does other convective condensate.

This coupling between the GCM's cumulus and stratiform cloud parameterizations has a dramatic effect on mean cloud water contents in the tropical upper troposphere (Fig. 4) and also produces realistic tropical cloud forcing variability (see section 4c). With the cloud water budget and anvil detrainment, convective

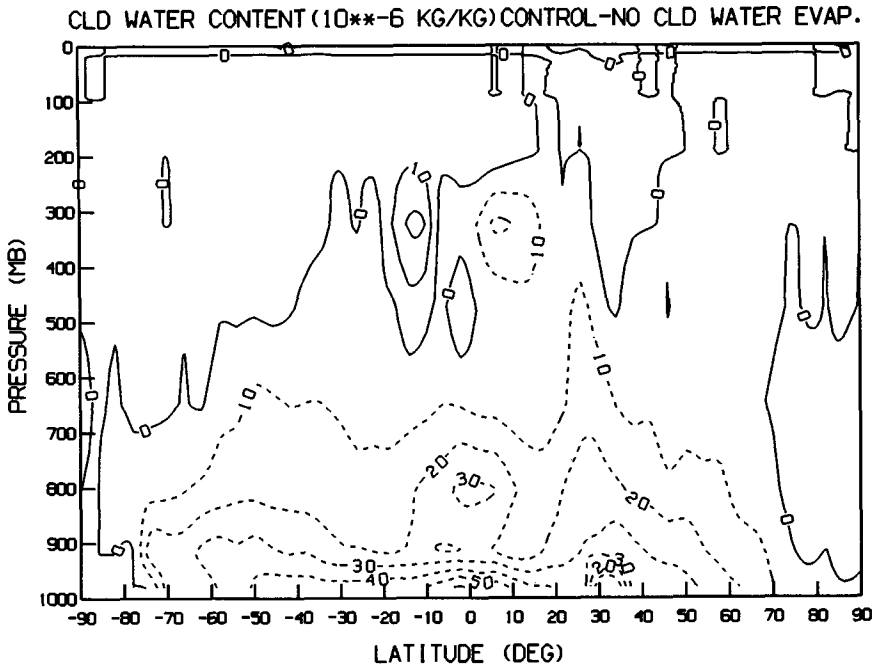

FIG. 3. Zonal mean difference in January cloud water content (10^{-6} kg kg^{-1}) between the GCM control run and a sensitivity experiment with no evaporation of cloud water.

clusters in the GCM can have finite life cycles, with the anvil persisting after the convection has ceased. Examination of histograms of the lifetimes of tropical convective systems simulated by the GCM indicates that more of them have high cloud persisting for 2–7 h after the initiation of deep convection than is the case when the Model II diagnostic cloud parameterization is used.

Although dilution by entrainment is crudely accounted for by our cloud water evaporation parameterization (17), in certain situations entrainment may catastrophically dissipate a cloud deck as a result of cloud-top entrainment instability (CTEI). Unfortunately, the proper instability criterion for CTEI and its importance relative to other breakup mechanisms are a matter of considerable controversy. Randall (1980) and Deardorff (1980) derived an instability criterion based on the ratio of the equivalent potential temperature jump, or equivalently the moist static energy jump Δh, across the cloud-top interface to the jump in total water content $\Delta(q + m/b)$. Defining $\gamma = (L/c_p)(\partial q_s/\partial T)_p$, $\delta = 1/\epsilon - 1 = 0.608$, $\kappa = c_pT/L$, and $\beta = [1 + (1 + \delta)\gamma\kappa]/(1 + \gamma)$, the criterion for CTEI can be written

$$k = \Delta h/L\Delta(q + m/b) > k_{\min}, \qquad (19)$$

where $h = c_pT + gz + Lq$ and

$$k_{\min} = \kappa/\beta \approx 0.23. \qquad (20)$$

But observations of the transition from marine stratus/stratocumulus to scattered trade cumulus suggest that nearly overcast conditions persist even when (19)–(20) is satisfied (Kuo and Schubert 1988). Kuo and Schubert suggest that the instability criterion is correct, but that slow growth rates in the marginal instability regime allow the cloud deck to survive for several hours. Betts and Boers (1990) suggest a transition at $k \approx 0.53$ instead on the basis of the available observations. MacVean and Mason (1990) and Siems et al. (1990) argue, however, that the criterion (19)–(20) is incorrect, and derive more restrictive instability criteria. The MacVean–Mason approach, for example, yields

$$k > k_{\max} = \frac{(1 + \gamma)[1 + (1 - \delta)\kappa]}{2 + [1 + (1 + \delta)\kappa]\gamma} \approx 0.70. \qquad (21)$$

Recent numerical simulations by MacVean (1993) suggest a continuum of possibilities, with liquid water e-folding times of order 10^4 s when $k \approx k_{\min}$ and 10^3 s when $k \approx k_{\max}$.

Experiments with an early version of the cloud water budget parameterization produced the result that almost all low cloud was dissipated in the Tropics and subtropics when (19)–(20) was used as an instability criterion. Thus, based on the available evidence, we have implemented the following parameterization for CTEI. When $k > k_{\min}$, we mix air between the cloud-top layer and the layer above in sufficient quantity to dissipate a fraction f of the cloud water in one physics time step Δt, with

$$f = 1 - e^{-\sigma(k)\Delta t} \qquad (22)$$

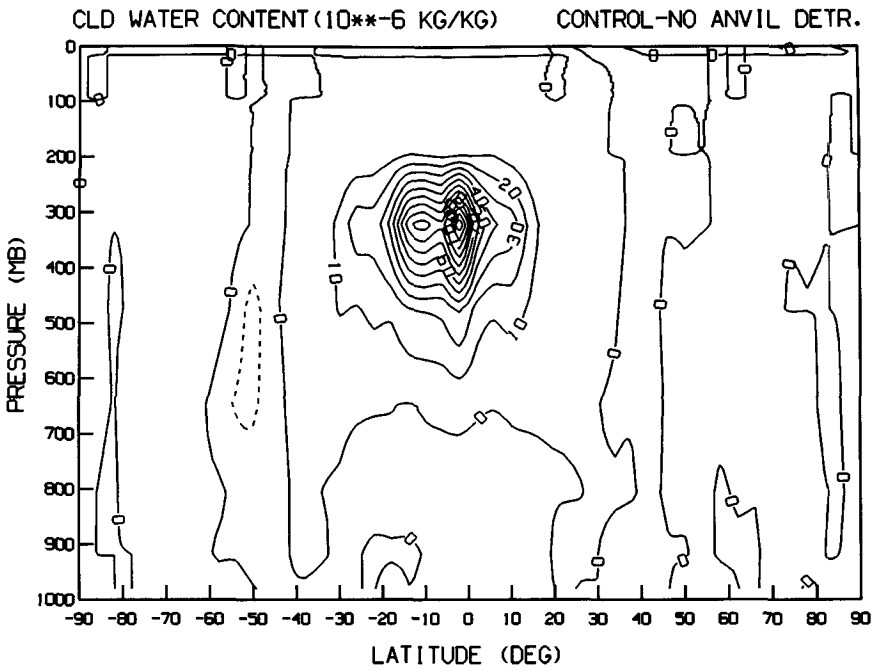

FIG. 4. As in Fig. 3 but for the difference between the control run and a sensitivity experiment with no detrainment of convective condensate from cumulus updrafts into stratiform anvil clouds.

and

$$\sigma(k) = 2 \times 10^{-4} \left(\frac{k - k_{\min}}{k_{\max} - k_{\min}} \right)^5 \text{s}^{-1}, \quad (23)$$

unless less mixing is sufficient to restore stability. Thus, $S_e = -fm/\Delta t$ is the CTEI cloud water sink in (3). The parameterization (22)–(23) allows for increasing cloud dissipation as k increases, but at a rate somewhat slower than in the simulations of MacVean (1993), since it acts in addition to the cloud water evaporation represented by (17). We allow CTEI to take place at any altitude, but it occurs almost exclusively in the first model level within the planetary boundary layer (PBL).

Figure 5 shows the geographical distribution of CTEI in the GCM. CTEI occurs mostly over the subtropical and tropical oceans (Fig. 5, top), with increasing frequency of occurrence with increasing distance from the west coasts of the continents. This is precisely the pattern expected for the stratocumulus-trade cumulus transition. Because of the restrictive instability criterion we use, however, the fraction of the cloud water mixed on average per physics time step is only 10%–30% of the total (Fig. 5, bottom). As a result, CTEI has only a moderate influence in the GCM in the current climate.

Because of the unique cloud dynamics of the PBL, we parameterize the cloud morphology as follows. When cloud exists in the first model layer, we set

$$b' = \begin{cases} 1 & (k < k_{\min}) \\ b + (1 - b)e^{-\sigma(k)\Delta t} & (k > k_{\min}) \end{cases} \quad (24)$$

for radiation purposes, while the optical thickness seen by radiation is

$$\tau' = \tau \frac{b}{b'}. \quad (25)$$

Equations (24)–(25) imply that the cloud fully occupies the gridbox horizontally in stable conditions, with the fractional cloudiness occurring only in the vertical. In very unstable conditions—$b' \to b$ and $\tau' \to \tau$—that is, the cloud is vertically developed and fractional cloudiness occurs only in the horizontal. If CTEI does not occur but moist convection originates in layer 1, we assume that $b' = b$ and $\tau' = \tau$ for any simultaneous stratiform clouds as in other GCM layers.

e. *Cloud radiative properties*

Given a prediction of the instantaneous cloud water content, we can allow the visible optical thickness to vary in a self-consistent manner. For the wavelengths and particle sizes of interest, the extinction efficiency is almost independent of size parameter, so the optical thickness takes the simple form

$$\tau \approx \frac{3\mu\Delta z}{2\rho_w r_e}, \quad (26)$$

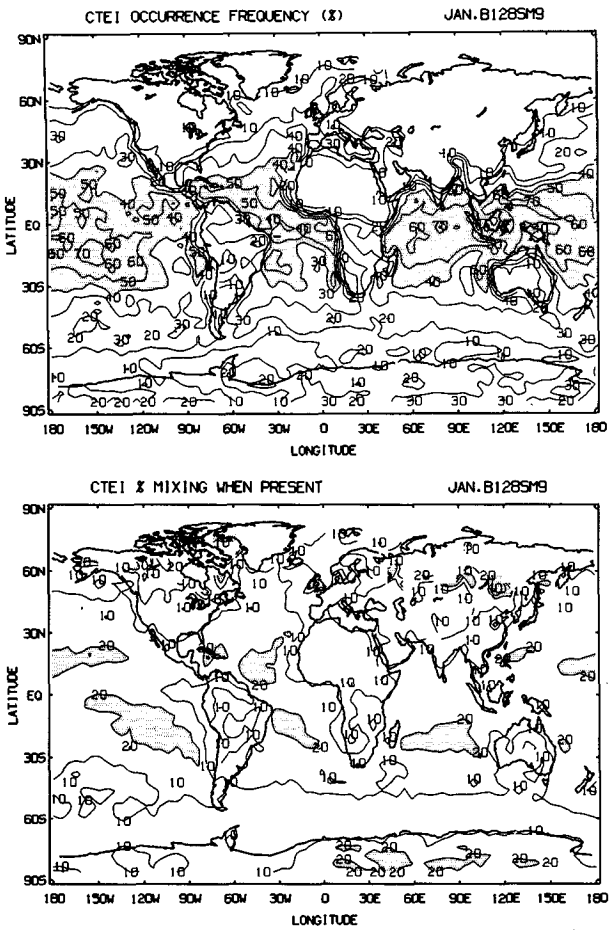

FIG. 5. Frequency of occurrence (%) of cloud-top entrainment instability between the first two model layers in the GCM in January (upper) and the mean fraction of liquid water mixed between the layers during CTEI occurrences (lower). Shading indicates occurrence frequencies > 40% in the upper panel and mixing fractions > 20% in the lower panel.

where Δz is the GCM layer physical thickness and r_e the effective radius of the droplet size distribution (Hansen and Travis 1974). Note that the cloud morphology prescriptions (9) and (25) are equivalent to assuming a cloud layer thickness of $b^{1/3}\Delta z$ and $(b/b')\Delta z$, respectively, rather than Δz in (26). Once the visible τ is estimated, infrared emissivity is then determined according to the spectral dependence predicted by Mie theory (Hansen et al. 1983), guaranteeing self-consistent shortwave and longwave radiative properties.

We diagnose particle size from the predicted cloud water content. Ignoring for simplicity the difference between the effective radius and volume-weighted mean droplet radius (r), the cloud droplet concentration N is given by

$$\mu = N\rho_w \frac{4}{3}\pi r^3 \tag{27}$$

for spheres. Observations suggest that for liquid phase clouds, constant N is a good approximation for low to moderate τ (Slingo et al. 1982; Han et al. 1994). This implies that r increases as $\mu^{1/3}$. We fit this behavior to data of Stephens et al. (1978), taking

$$r = r_0(\mu/\mu_0)^{1/3} \tag{28}$$

with $r_0 = 10$ μm at $\mu_0 = 0.25$ g m^{-3} (corresponding to $N \approx 60$ cm^{-3}) over ocean. Over land, where there are many more CCN, we set $r_0 = 7$ μm ($N \approx 170$ cm^{-3}) instead. For ice clouds, we fit (28) to the data of Platt (1989), although the fit is less satisfactory. Fewer particles act effectively as ice nuclei, so ice crystals tend to be larger than liquid droplets. We use $r_0 = 25$ μm at $\mu_0 = 4.2 \times 10^{-3}$ g m^{-3} ($N \approx 0.06$ cm^{-3}) for all ice clouds. In this case r is the radius of an equivalent sphere; that is, the Mie scattering phase function is used. The data of Nakajima et al. (1991) and Han et al. (1994) suggest that r for liquid clouds does not increase indefinitely with μ, perhaps due to the onset of precipitation. We therefore set $r = r(\mu_r)$ when $\mu > \mu_r$ for liquid clouds. Equation (28) is also used in calculating the cloud droplet evaporation rate (15); that is, we ignore the difference between effective and mean radius.

Frequency histograms of effective radius resulting from this parameterization are shown in Fig. 6. The mean low cloud liquid droplet radius is about 8 μm over ocean and 6 μm over land, but the distribution is broad. The cutoff at 14 μm represents the efficient precipitation threshold; this threshold is more commonly reached for marine clouds, which precipitate more easily, than for continental clouds. Low-level ice clouds, for which data are sparse, typically have quite large particle sizes (40–80 μm). High-level ice clouds exhibit a bimodal distribution, with a peak near 60 μm due to thick cumulus anvil clouds (mostly occurring near the anvil base) and a 5–15 μm population of thin cirrus. The diagnosed effective radii for low liquid and high thin ice clouds are somewhat smaller than observed (Han et al. 1994; Wielicki et al. 1990) for several reasons. 1) We do not distinguish between volume-weighted mean radius and effective radius; (27)–(28) are more appropriate to the former. For a standard gamma distribution of droplet size with an effective variance of 0.2, a typical value for stratus, $r_e \approx 1.3r$ (Han et al. 1994). 2) The parameterization depends on the predicted liquid water content μ; we show in the next section that the current GCM underpredicts liquid water path (the vertical integral of μ) relative to microwave-retrieved values in several regions of thick cloudiness.

3. Mean state

Energy balance and hydrologic cycle parameters simulated by the model are listed in Table 1. Global top-of-the-atmosphere (TOA) radiation budget and

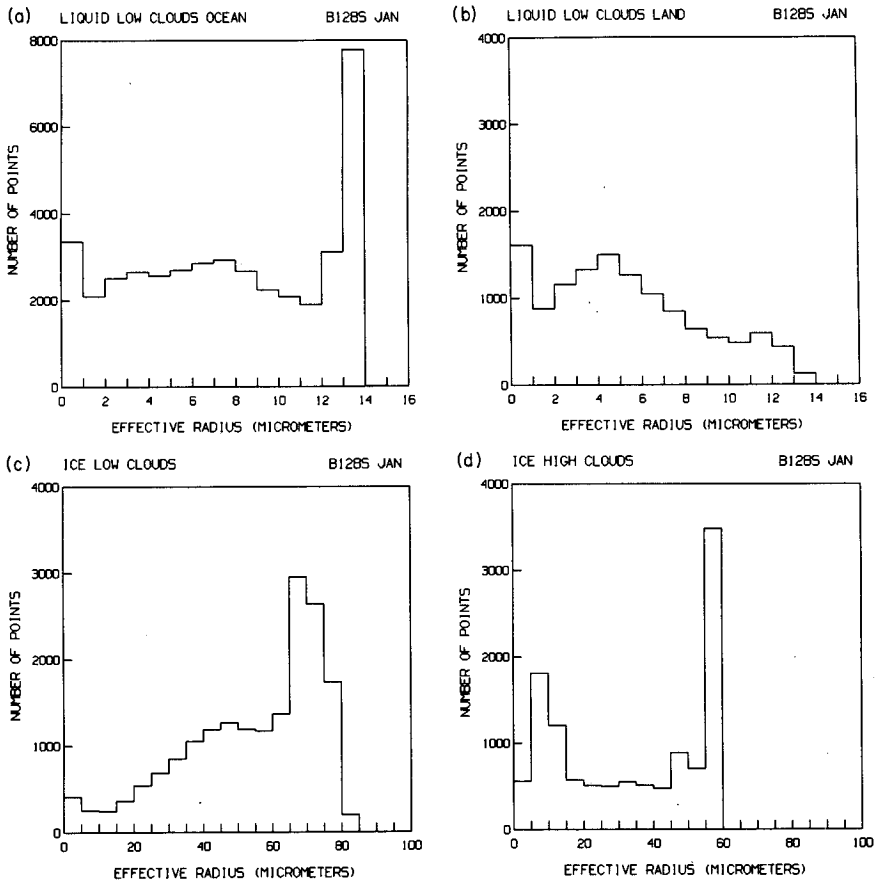

FIG. 6. Frequency histogram of cloud particle effective radius (μm) occurrence diagnosed in the GCM in January for (a,b) liquid phase low-level clouds over ocean and land, respectively, (c) ice phase low-level clouds, and (d) ice phase high-level clouds.

cloud forcing components are within 5 W m^{-2} of observations except for longwave cloud forcing, which is 5–10 W m^{-2} weaker than that inferred by *Nimbus-7* and about 15 W m^{-2} less than that retrieved by the Earth Radiation Budget Experiment (ERBE). About half the discrepancy is due to the GCM's underestimate of high cloud cover (see section 5). The remainder may be an observational bias, because satellite-derived cloud forcing includes the effect of higher humidities within clouds; the GCM performs offline clear sky calculations even in cloudy gridboxes and thus isolates the true cloud effect. TOA and surface shortwave cloud forcing are almost identical in the GCM.

Total cloud cover in the GCM is a few percent less than that estimated by the International Satellite Cloud Climatology Project (ISCCP), with most of the underestimate occurring over ocean. The GCM correctly simulates the large land–ocean difference in total cloud cover but not the significant January–July difference over land, for reasons that will be discussed later. Low cloud cover is larger than estimated by surface observers by about 5%, and high cloud cover lower than estimated by ISCCP by the same amount. The GCM is generally too dry and too cold in midlatitudes, especially in the middle and upper troposphere; it is somewhat too wet in the tropical upper troposphere. Liquid water path is somewhat smaller than observed, although the uncertainty in the data is large. Liquid water path is greater than or comparable to ice water path in the subtropics, but the ice phase dominates elsewhere. Precipitation by stratiform clouds accounts for about one-third of the total globally, and about 15% near the equator; the latter is less than estimated from budget studies of tropical cloud clusters, but a great improvement over Model II, which has no mechanism for condensate detrainment into anvils and thus has virtually no stratiform precipitation in the Tropics.

Figures 7–13 display the geographic distributions of several GCM-simulated quantities and differences between the GCM and observations, including TOA-absorbed shortwave and outgoing longwave radiation (ASR, OLR; differences only), TOA shortwave and longwave cloud forcing (C_s, C_l), total, high, and low cloud cover (TC, HC, LC), and cloud liquid water path

TABLE 1. Selected climate parameters simulated by the GCM with the prognostic cloud water parameterization. All quantities are global unless otherwise indicated.

	Annual	January	July
TOA energy balance (W m^{-2})			
Net radiation	3.6	11.6	−6.1
Absorbed shortwave	238.2	244.0	231.3
Net longwave	−234.7	−232.4	−237.4
Shortwave cloud forcing	−53.7	−57.8	−51.3
Longwave cloud forcing	16.9	16.3	17.4
Surface energy balance (W m^{-2})			
Net energy into surface	3.0	10.0	−7.2
Absorbed shortwave	172.3	176.8	166.0
Net longwave	−55.6	−54.3	−55.1
Latent heat flux	−88.8	−89.3	−91.2
Sensible heat flux	−23.7	−21.8	−25.9
Shortwave cloud forcing	−54.2	−58.6	−51.5
Longwave cloud forcing	20.8	21.9	19.7
Cloud cover (%)			
Total (global/land/ocean)	57/45/61	58/50/61	56/43/62
High	15	15	16
Middle	16	16	15
Low	47	49	46
Cloud water path (0.1 kg m^{-2})			
Liquid	0.9	0.9	0.9
Ice	1.5	1.4	1.6
Precipitation, global/land/ocean (mm d^{-1})			
Convective	2.0/1.8/2.3	2.0/1.7/2.3	2.1/2.0/2.3
Stratiform	1.0/0.9/1.1	1.0/1.0/1.1	1.0/0.8/1.1
Precipitable water (mm)	23.4	22.1	25.2
Specific humidity 2°/50°N (g kg^{-1})			
959 mb	14.8/4.6	14.6/2.9	14.6/7.3
634 mb	4.6/1.4	4.4/0.73	4.5/2.6
321 mb	0.49/0.10	0.45/0.04	0.46/0.24
Surface air temperature (°C)	14.0	12.2	15.6
Temperature 2°/50°N (°C)			
959 mb	22/4	22/−4	22/13
634 mb	5/−13	4/−21	4/−2
321 mb	−29/−45	−30/−52	−29/−36
102 mb	−75/−62	−76/−62	−74/−61

(LWP). ERBE data (Barkstrom 1984) are used to validate radiation quantities, ISCCP C2 and C1 data (Rossow and Schiffer 1991) for total and high cloud cover, respectively, the surface cloud observation dataset of Warren et al. (1986, 1988) for low cloud cover, and the SSM/I retrieval of Lin and Rossow (1994) for liquid water path.

It is important to note specific problems with individual datasets. ERBE cloud forcing is less accurate than its radiation fluxes because the former requires separation of cloudy and clear scenes. In the polar regions, cloud detection over snow and ice is sufficiently difficult to produce the incorrect sign of cloud forcing (Cess, 1994, personal communication); we restrict comparisons to latitudes equatorward of 60°. ISCCP also has a detection problem over snow and ice, but of unknown magnitude; we return to this question later. Surface cloud observations are of poorer quality over lightly traveled ocean regions, such as the southern midlatitudes, than over land. SSM/I liquid water path is available only over ocean because of the variable microwave surface emissivity of land. Retrievals by different groups differ completely, even as to the sign of the latitudinal gradient (Lin and Rossow 1994). In heavily precipitating regions, the retrieved liquid water path includes a partial contribution from precipitation-sized droplets. For the GCM, only the cloud water path is included; for convective clouds, whose cloud water content is not predicted, we convert the prescribed optical thickness for liquid parts of the cloud to a proxy liquid water path using a relation suggested by Lin and Rossow. Nonetheless, model–data discrepancies in this quantity in the ITCZ should be viewed with caution.

The TOA radiation balance (Fig. 7) represents the integrated effect of all elements of the simulated climate, and Figs. 8–13 permit us to understand these model–data differences in terms of individual cloud types and/or hydrologic/radiative quantities. Differences between cloud-forcing errors (Figs. 8–9) and TOA radiation errors provide a qualitative measure of clear-sky contributions to the total TOA radiation error; these differences are significant only in the longwave. Additional validation of the GCM's upper-troposphere water vapor distribution against SAGE II data can be found in Del Genio et al. (1994). We organize the discussion below according to different climate regimes in which different cloud types dominate the radiation signature.

(*i*) *Tropical convection regions:* The GCM overestimates the magnitude of C_s in the ITCZ, especially over ocean. Low cloud cover is too high over the tropical oceans, while HC is slightly overestimated, but not sufficiently to explain the total C_s error. LWP is underestimated, but the data are very uncertain here. This suggests that either model anvil clouds contain too much ice or that excessive low cloudiness contributes too much to C_s. Here C_l is generally underestimated, but not always in the regions of the maxima in C_l and C_s, while both positive and negative OLR errors occur. This is probably due to errors in the exact location of convective centers and the model's excessive upper-troposphere humidity.

(*ii*) *Subtropical/tropical ocean subsidence regions:* These areas, off the west coasts of North America, South America, and Africa, are dominated by low-level marine stratus, which have a noticeable shortwave effect and little longwave signature. The GCM underestimates TC, mostly due to insufficient LC, and thus underestimates C_s in these regions, more so in July than January. This occurs despite the relative absence of CTEI in these regions (Fig. 5). LWP errors are within the observational uncertainty, which illus-

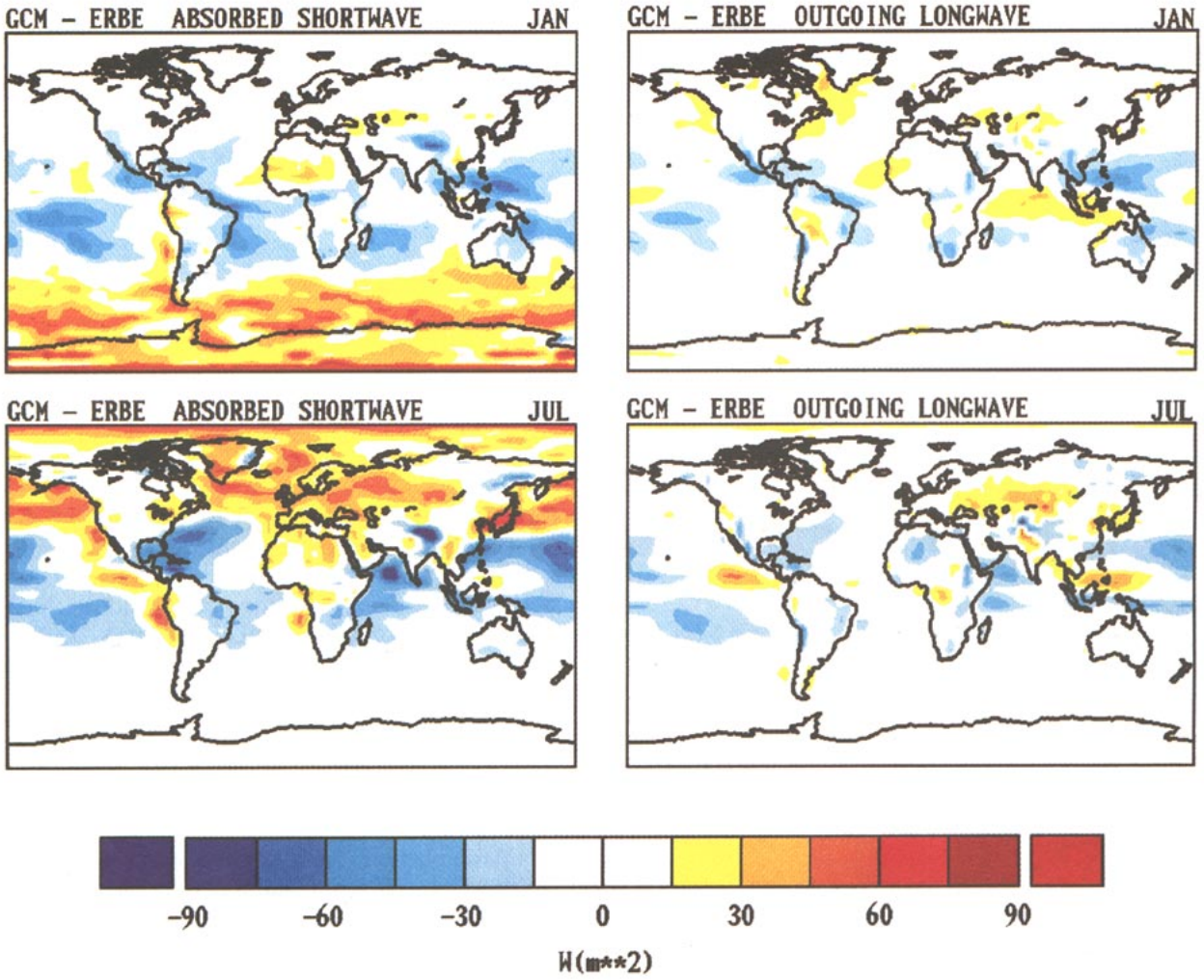

FIG. 7. Differences between GCM-simulated and ERBE-observed TOA absorbed shortwave (left) and outgoing longwave (right) radiation flux for January (top) and July (bottom). The GCM results are 5-yr averages with climatological SST; the ERBE data cover January 1986–1989 and July 1985–1988. OLR is defined as positive in this figure.

trates that the microwave is not very sensitive to thin clouds.

(*iii*) *Subtropical/midlatitude continents:* The major deficiency in the GCM's cloud simulation occurs over Eurasia. In January, excessive TC is simulated, most of it due to excessive LC, in northern/eastern Eurasia. This is a problem common to many GCMs (Mokhov, 1994, personal communication). In July, to the west and at somewhat lower latitude, TC, LC, and C_s are all greatly underestimated. This may have several causes, including the underestimate of shallow cumulus over land by the GCM's convective scheme (see section 4a) and the underestimate of potential evapotranspiration by the GCM's land surface parameterization. There is also slightly too much OLR and too little C_l and HC in these regions, also suggestive of a deficient local surface moisture source. It is this region that accounts for the GCM's incorrect seasonal cycle of global mean continental cloud cover (see also section 4b).

(*iv*) *Midlatitude storm tracks:* The GCM underpredicts C_s, TC, and LWP off the east coasts of North America and Asia and throughout the Southern Hemisphere midlatitude oceans. Here HC errors are large relative to LC errors, and C_l is too low as well, which suggests deficiencies in baroclinic storm-generated nimbostratus. The middle and upper troposphere are substantially drier here than in observations. Errors in OLR are smaller than those in C_l, despite the low humidity, presumably because upper-troposphere temperature is too low at these latitudes. Reduction of 5–10 W m^{-2} in ASR is realized when the model's cloud overlap is changed from maximum to effectively random, but the remaining error is insensitive to large changes in the parameterization's microphysical con-

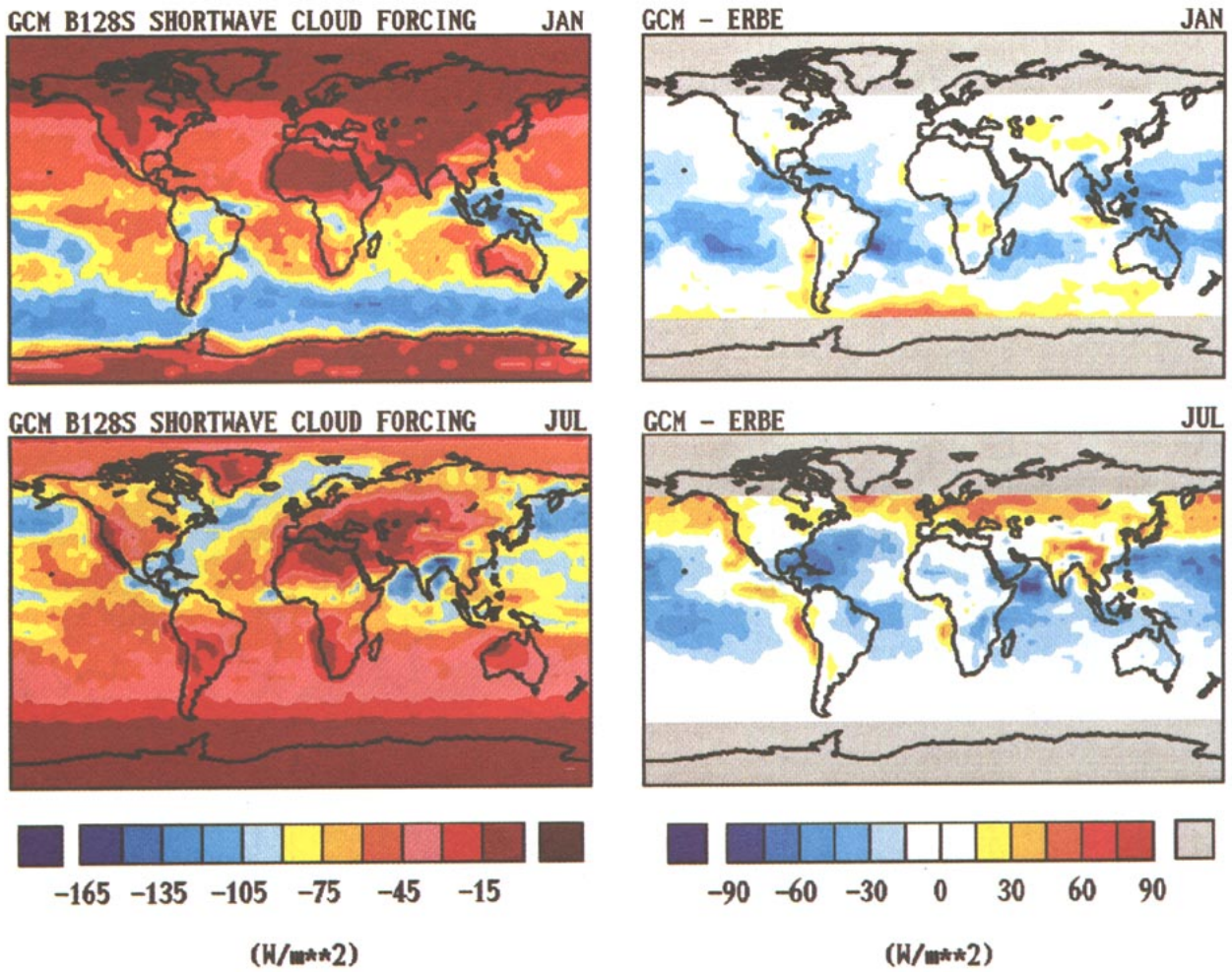

FIG. 8. GCM-simulated shortwave cloud forcing (left) and GCM-ERBE differences (right) for January (top) and July (bottom). The GCM results are January 1985–1988 and July 1985–1988 averages from an AMIP simulation; gray areas indicate missing/excluded data.

stants. A large reduction in U_{00} produces improvement but seriously degrades the tropical cloud simulation. There are several reasons to suspect that this problem lies outside the cloud parameterization. The underestimate of water vapor is completely insensitive to any change in the cloud parameterization; the primary water vapor source in the GCM's budget at these latitudes is transport by large-scale eddies (Del Genio et al. 1994). However, upper-troposphere eddy kinetic energy is about 30% lower than observed, despite the fact that the new parameterization increases eddy kinetic energy and baroclinic conversion (see Table 2). Furthermore, a sensitivity experiment in which the new cloud and convection schemes are combined with the previous Model II dynamics, PBL, and land surface parameterizations produces about twice as much midlatitude high cloudiness.

(*v*) *Polar regions:* These are presumably regions of primarily boundary layer and midtroposphere cloudiness, but few data exist. The only unambiguous validation statement that can be made is that the GCM overestimates ASR in the summer polar region, but snow/ice coverage and albedo errors contribute to this to an unknown extent. Much of the error is likely to be due to clouds, however, since the ASR difference is an extension of that in midlatitudes. According to ISCCP, though, the GCM greatly overpredicts TC at the summer pole; either the data are unreliable here, or the simulated optical thicknesses are much too small; we will return to this point later. At the winter pole, the model underpredicts TC according to ISCCP, but again, uncertainties are large.

Further insight into these differences can be gained by examining the cloud radiative properties directly. Figures 14–16 compare simulated and ISCCP-observed (Rossow and Schiffer 1991) two-dimensional histograms of cloud-top pressure and optical thickness for January in selected latitude zones. To compare the GCM to ISCCP, we must take into account biases in

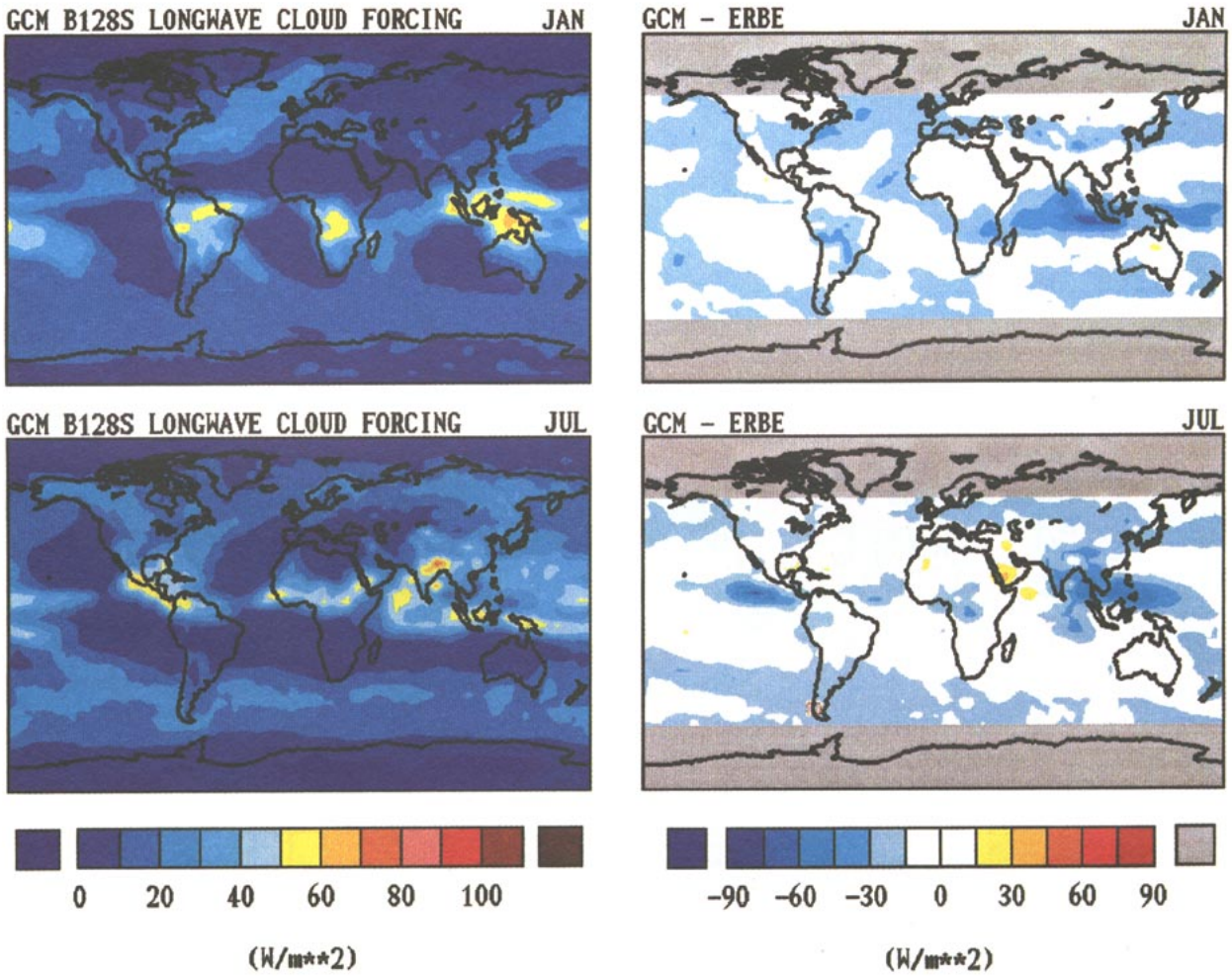

FIG. 9. As in Fig. 8 but for longwave cloud forcing.

cirrus clouds produced by the ISCCP cloud retrieval algorithm: 1) it neglects the non-sphericity of ice crystals (as does the GCM) and underestimates their particle size, 2) it misses extremely thin cirrus and cannot unambiguously determine the cloud-top pressure of the thinnest clouds it does detect, and 3) it does not sufficiently correct upward the cloud-top pressures of slightly optically thicker clouds. These differences have been quantified by Liao et al. (1995b) by comparisons between nearly coincident SAGE II and ISCCP pixels. Using these results as a guideline, we "detect" the highest cirrus layer in the GCM as ISCCP would, by ignoring clouds with $\tau < 0.1$, placing clouds with $0.1 < \tau < 0.3$ at the tropopause (as ISCCP does when it cannot determine a cloud-top pressure), and placing clouds with $0.3 < \tau < 0.5$ one model layer lower than that at which they actually occur. Furthermore, the GCM is "viewed" top down as the satellite would see it, with only the top pressure of the highest cloud in the column included. The GCM figures are thus an approximation of the ISCCP "detection" of the GCM cloud field rather than the actual GCM cloud distribution. ISCCP also underestimates the optical thickness of low clouds in cases of subpixel (<5 km) fractional cloudiness, but this is difficult to quantify and has not been taken into account in the figures.

Over the tropical oceans (Figs. 14a,b), the GCM correctly simulates the bimodal optical thickness distribution of high clouds due to deep convection, thick anvils, and associated cirrus. This suggests that the GCM's overestimate of C_s (Fig. 8) at these latitudes is due more to its overestimate of low cloud cover than to an overestimate of ice water content (but see the discussion in section 6). ISCCP observes cloud-top pressures systematically increasing with decreasing τ, while the GCM's high clouds peak near 250 mb, independent of τ. The GCM and ISCCP agree that the dominant cloud type at these latitudes is low-level stratus, with tops near 900 mb. The GCM's optical thicknesses are systematically higher than ISCCP's, but whether this is a real discrepancy or an ISCCP bias is

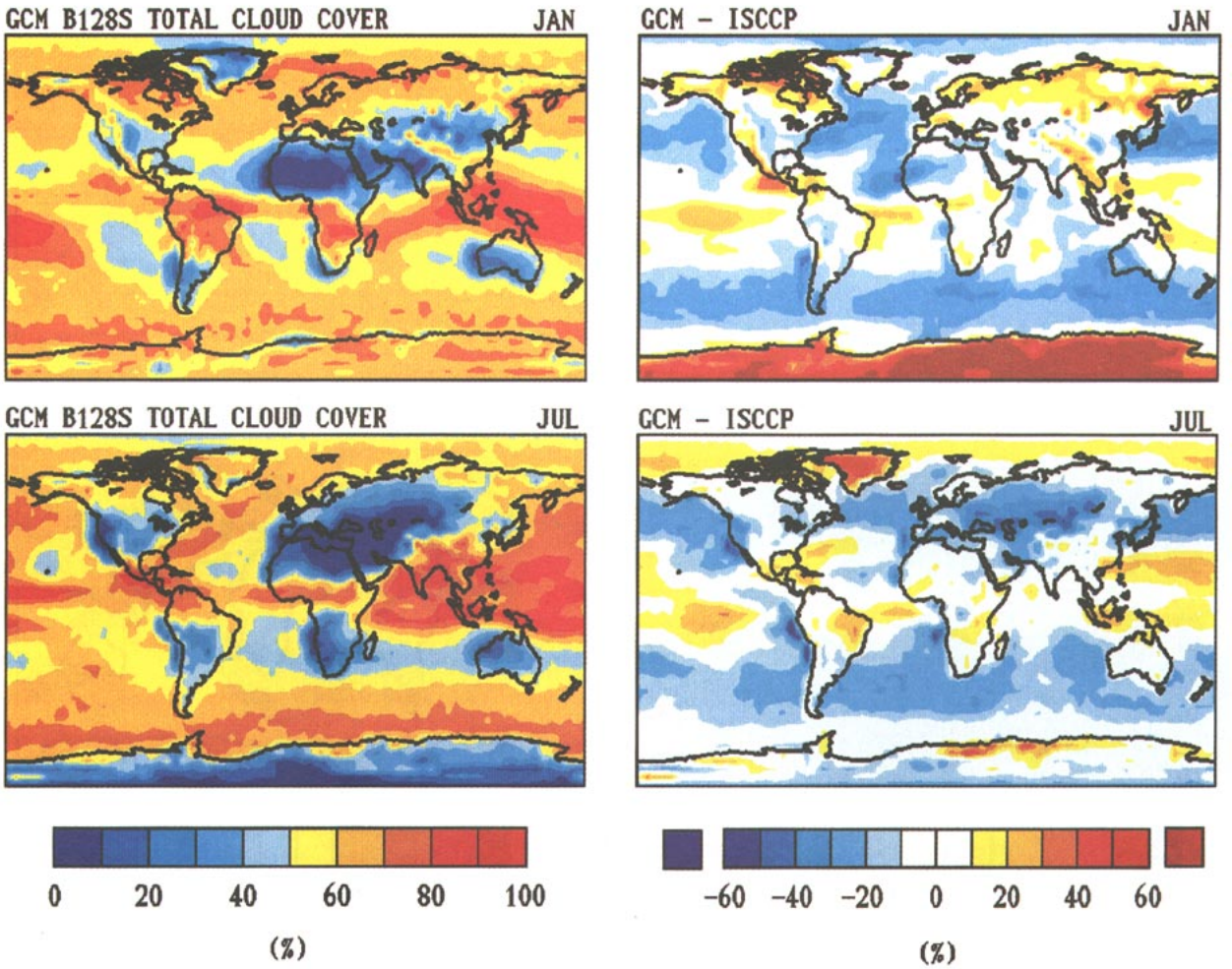

FIG. 10. As in Fig. 8 but for total cloud cover (%) and GCM-ISCCP differences. The GCM results are 5-yr averages with climatological SST; the ISCCP data are averaged over July 1983–1989 and January 1984–1989 from the C2 dataset.

not known; if it is real, then it contributes to the excessive tropical C_s.

Over subtropical oceans (Figs. 14c,d), the same low-level stratus cloud type is even more dominant in both model and data. This supports our earlier conclusion that the GCM's underestimate of C_s in the eastern ocean marine stratus decks is mostly due to an underestimate of low cloud cover (Fig. 12). There is also a tendency for optically thicker low clouds at slightly lower top pressures; in the data these are probably trade cumulus (750-mb tops), but in the GCM, which underpredicts shallow convection (see section 4a), these are probably thicker stratus (850-mb tops) instead. Both model and data indicate a broad secondary distribution of high-level clouds, but the top pressures are 100–150 mb lower in the GCM than in ISCCP.

Midlatitude winter continental cloudiness consists primarily of midlevel optically thick clouds, typical of nimbostratus, with secondary peaks due to thin cirrus, midlevel moderate τ cloudiness (perhaps altocumulus or altostratus), and a hint of moderate τ stratus at low levels (Figs. 15a,b). The GCM identifies each of these cloud types, but simulates too much low stratus and too little nimbostratus. This is consistent with our earlier conclusion of excessive low cloudiness in winter over Eurasia. Over midlatitude oceans (Figs. 15c,d), the GCM simulation is fairly good relative to ISCCP, but with the same problem as in the Tropics of similar top pressures for optically thick and thin high clouds. The GCM distribution is too heavily weighted toward low clouds, which suggests that the underprediction of C_l, C_s, TC, HC, and LWP in the storm tracks is due to nimbostratus occurring too infrequently, rather than their optical properties being incorrect. The weakness of the GCM's synoptic storms is consistent with this conclusion.

The GCM predicts a bimodal distribution of Arctic cloud types in daytime in both summer and winter (Figs. 16a,b). In both seasons the model's primary cloud type is low stratus, but more so in summer. In

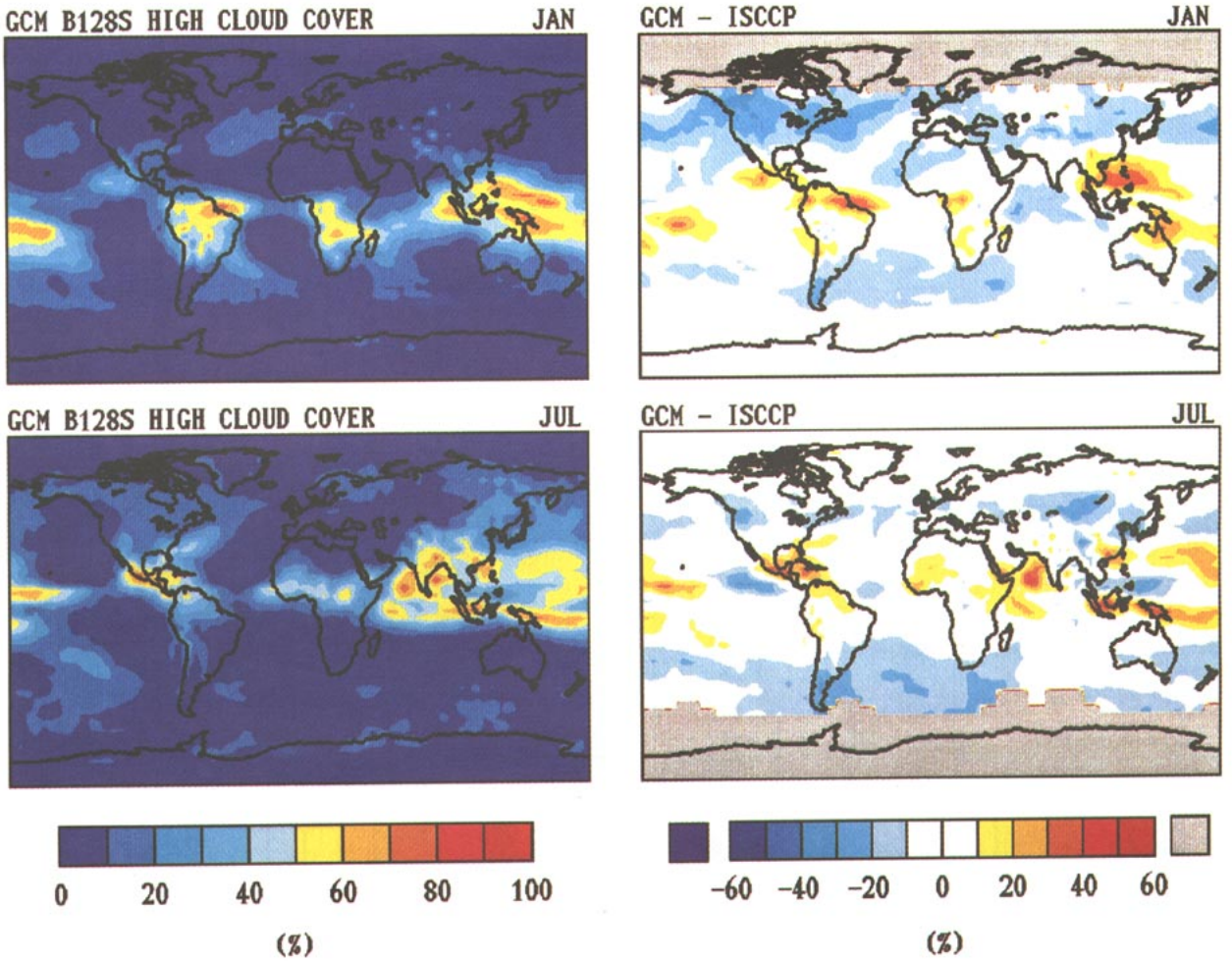

FIG. 11. As in Fig. 10 but for high cloud cover; the ISCCP data are averages over 1985–1990 using visible-IR detection thresholds from the C1 dataset.

both seasons these clouds have a broad optical thickness distribution, but in winter there is more optically thin cloudiness. The secondary peak in both seasons is at midlevels, slightly higher in altitude in summer than winter and somewhat optically thicker as well. The winter distribution of nighttime cloudiness (not shown) at both low and midlevels peaks at even lower values of τ. ISCCP does not obtain τ information in winter because of the absence of sunlight, but its Arctic summer distribution completely disagrees with the GCM, with primarily optically thick midlevel cloud and thin cirrus and almost no boundary layer cloudiness (Fig. 16c). Curry and Ebert's (1992) tentative Arctic seasonal climatology suggests a bimodal (low and midlevel) distribution of clouds and τ varying from about 2 in winter to about 8 in summer. The GCM is in reasonable agreement with this estimate, casting doubt on the ISCCP inference. GCM clouds over Antarctica in summer (not shown) are more like those in Arctic winter, but with even optically thinner low cloudiness. This too disagrees with ISCCP, whose Arctic and Antarctic clouds (not shown) are similar.

Liao et al. (1995a) have examined the thin cirrus not seen by ISCCP but detected by SAGE II. They find that thin cirrus cloud amounts are typically 10%–20% in the Tropics and summer midlatitudes, and 5%–10% elsewhere. If thin cirrus are defined in the GCM as all clouds with top pressures < 550 mb and column $\tau < 0.1$ down to this level, then the GCM produces significantly less thin cirrus: 3%–6% in the Tropics, 0.5%–2% in the subtropics and summer midlatitudes, and 0.1%–4% in the winter midlatitudes. A cutoff $\tau < 0.3$ approximately doubles these amounts. The GCM's upper-level dry bias must play a role in the midlatitude deficiency of thin cirrus, but this cannot be said for lower latitudes, which are somewhat too moist. One possibility is that the GCM's coarse vertical resolution near the tropopause (2–3 km) prevents the formation of thin, stable, moist layers in which cirrus are commonly observed to form (Starr and Wylie 1990).

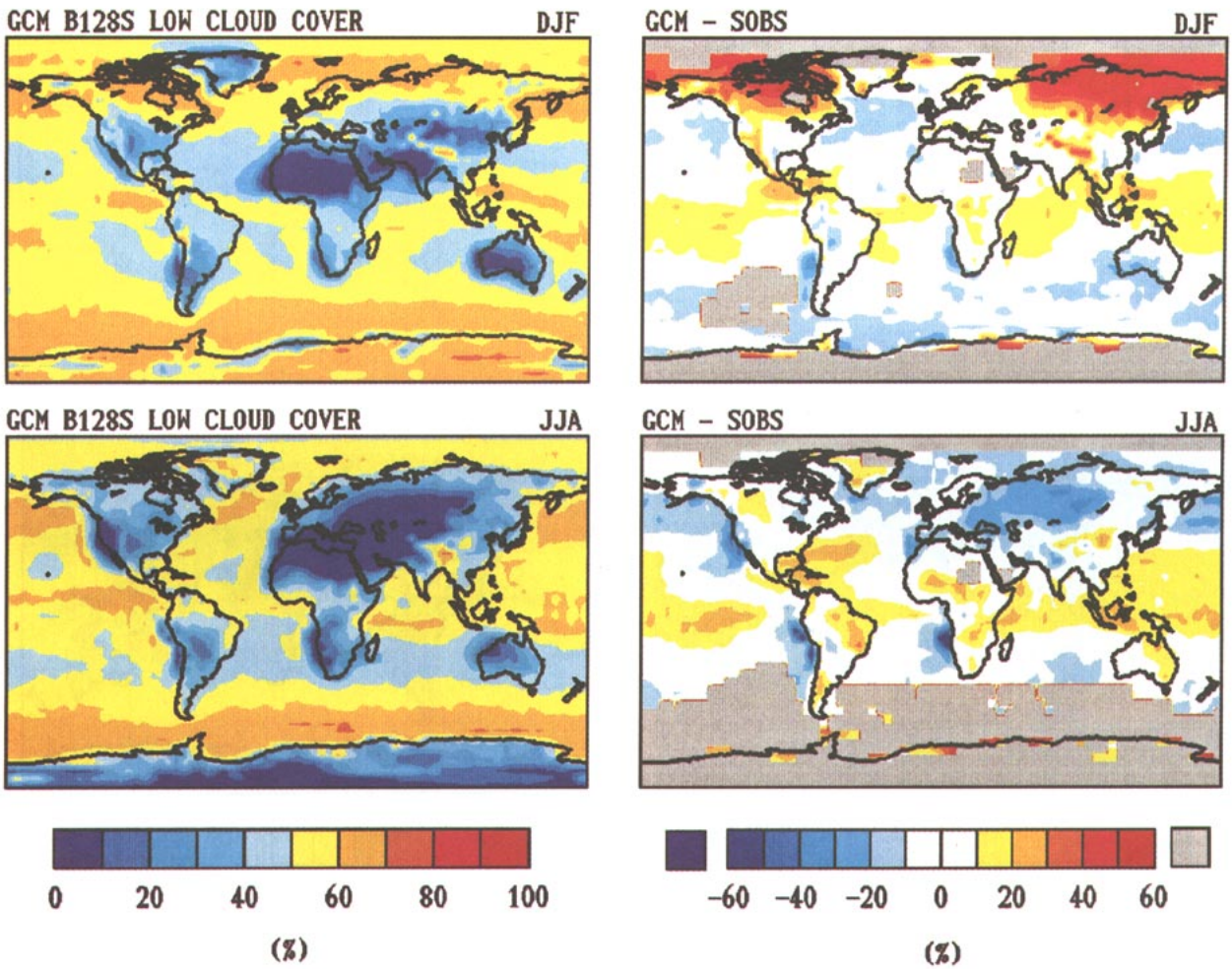

FIG. 12. As in Fig. 10 but for seasonal average (Dec.–Jan.–Feb. and Jun.–Jul.–Aug.) low cloud cover and differences relative to surface cloud observations. The data are averages over 1971–1981 for land points, and over 1952–1981 for ocean points; gray areas indicate missing/insufficient data.

Table 2 compares various indices of the GCM's general circulation with those from a one-year sensitivity experiment in which the prognostic scheme was replaced with the previous Model II diagnostic cloud parameterization. All other model physics is identical in the two runs. The prognostic version has a more vigorous hydrologic cycle, with increased precipitation, evaporation, and cumulus mass flux. This produces a stronger general circulation, with intensified Hadley and Ferrel cells and increased eddy kinetic energy; each improves the model's agreement with observations (Oort 1983). Large-scale energy transports increase as well, primarily due to increases in latent heat transports.

To understand these results, we examine the January zonal mean changes in cloud cover and diabatic heating that result from the change in cloud parameterization (Fig. 17). The prognostic scheme dramatically increases low- and middle-level cloud cover in the Tropics and subtropics, while generally decreasing high-level tropical cloud cover and all types of cloudiness at higher latitudes (Fig. 17a). The changes in cloud cover are due primarily to increases/decreases in water vapor concentration (not shown) at high/low temperatures rather than changes in temperature itself. Temperature differences (not shown) are small with two exceptions: the prognostic scheme cools the tropical tropopause by 4°C and warms the winter polar region by 3°–6°C, both improvements. There may be several reasons for the change in the moisture field. Temperature-dependent cloud water evaporation (Fig. 3) is one candidate. Given the longer residence time of cloud water in a prognostic scheme, there is more opportunity for condensate to evaporate before it precipitates. In the diagnostic Model II scheme, cloud water is instantly converted to precipitation, and thus has only one chance to evaporate. In addition, CTEI provides a net increase in atmospheric humidity by removing moisture to the top of the PBL; the loss of near-surface moisture by

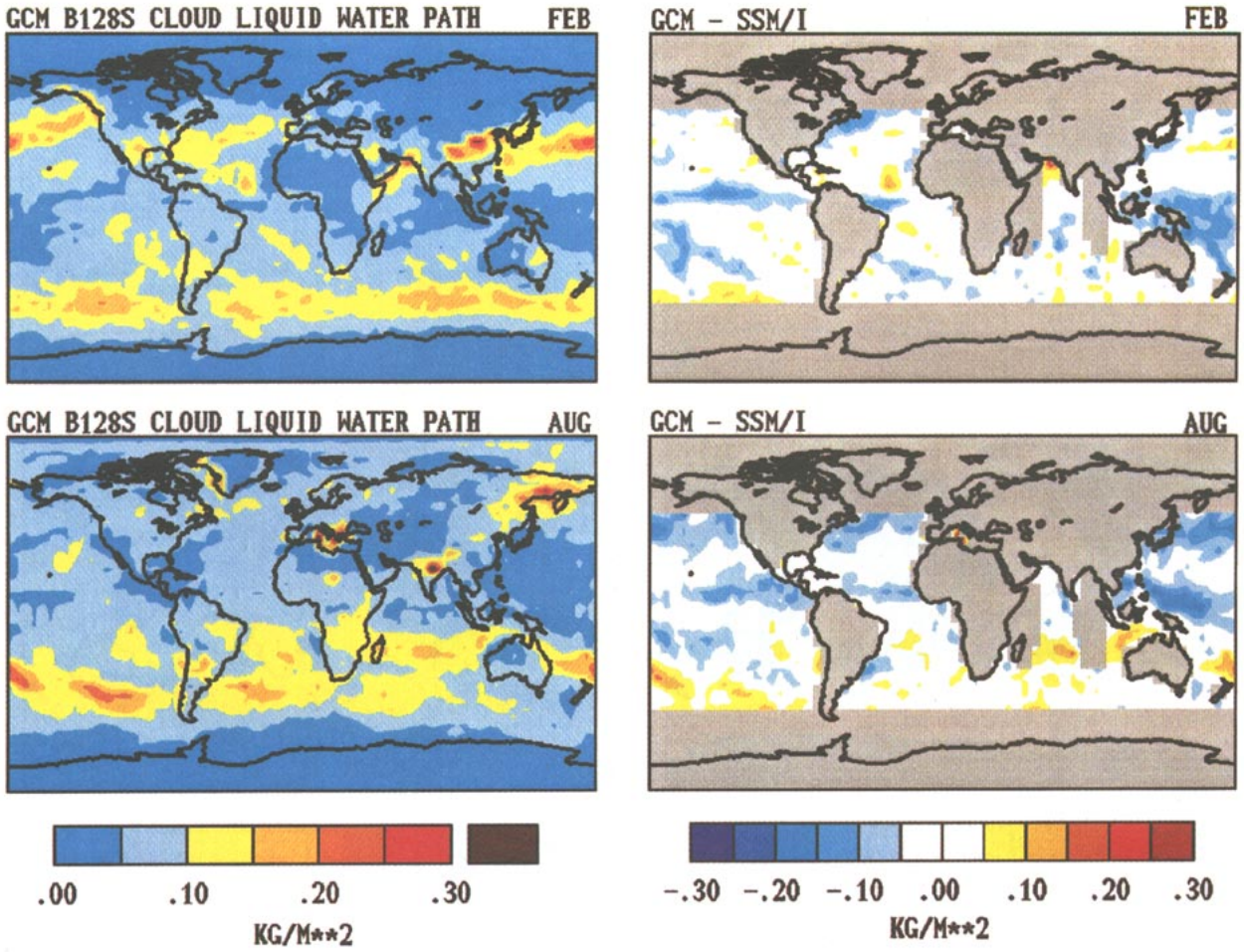

FIG. 13. As in Fig. 10 but for February and August cloud liquid water path and differences relative to SSM/I. The data are for 1987; gray areas indicate missing/insufficient data.

entrainment mixing is balanced by increased surface evaporation.

With a steeper humidity profile at almost all levels and more low cloud, there is generally increased longwave flux divergence in the Tropics and hence stronger radiative cooling at low latitudes (Fig. 17b). Shortwave heating differences are less dramatic, but reduced solar heating (due to optically thick anvils) helps produce the colder tropical tropopause. This decrease in the latitudinal gradient in radiative heating is more than compensated, however, by the increased tropical moist convective heating (Fig. 17c) driven by the wetter lower troposphere and a slightly steeper lapse rate. The change in cumulus heating is partly offset by stratiform cloud water evaporation (Fig. 17d) in the middle and lower troposphere, but it is augmented in the upper troposphere by condensation heating associated with anvil cloud formation. The net result is an increased latitudinal gradient of tropical diabatic heating and a stronger Hadley cell.

In midlatitudes, enhanced latent heat transport is due to both the steeper humidity gradient and the increased transient eddy kinetic energy (EKE). This occurs despite the fact that temperature increases at high latitudes, thus decreasing baroclinicity. In the face of smaller meridional temperature gradients, the stronger midlatitude eddies exist only because of increases in condensation heating there and associated enhanced longwave heating (Fig. 17b,d). Since mean cloud cover decreases in midlatitudes, the stronger eddies may indicate more favorable correlations between cloud processes and regions of rising motion. As evidence, eddy generation of available potential energy (APE) at 45°N increases by 6% with the new scheme, with a larger condensation contribution more than offsetting an increase in the (negative) radiation contribution. This may be caused by both the variable optical thickness and suppressed autoconversion in regions of rising motion (11). As a result, conversion of APE to EKE increases by 40%.

TABLE 2. Selected diagnostics of the general circulation in January simulations with the new prognostic cloud parameterization and the GISS Model II diagnostic cloud parameterization. All quantities are global means unless otherwise indicated.

	Prognostic	Diagnostic
Cumulus mass flux (10^9 kg s^{-1})	1361	1161
Peak N. H. streamfunction (10^9 kg s^{-1})		
Hadley cell/Ferrel cell	177/26	168/17
Diabatic heating (10^{14} W)		
Radiation	−566	−512
Moist convection	384	330
Stratiform phase changes	81	71
Surface sensible heating	111	122
N. H. poleward transport by eddies (10^{14} W)		
Dry static energy	17.9	18.1
Latent heat	11.6	10.0
N. H. upward transport by eddies (10^{14} W)		
Dry static energy	13.1	12.9
Latent heat	15.5	13.1
N. H. tropospheric energy (10^5 J m^{-2})		
Available potential (APE)	89.9	91.0
Eddy kinetic (EKE), transient/stationary	6.9/2.6	5.3/2.4
Tropospheric energy conversions, 45°N (W m^{-2})		
Generation eddy APE	3.2	3.0
by radiation	−2.8	−2.0
by condensation	2.5	1.7
by surface fluxes	3.4	3.3
APE→EKE	5.5	4.0

4. Temporal variability

a. Diurnal cycle

Diurnal variations in cloudiness are often ignored in GCMs, and some GCMs inexplicably still do not even include the diurnal cycle of insolation. Yet it is possible to induce a cloud feedback without changing cloud cover merely by shifting the cloud cover maximum from day to night, or vice versa. Furthermore, diurnal cycles differ for different cloud types and thus provide a stringent test for GCM physics. We focus on diurnal variations in total and high cloud cover, which are observed by satellite and determine the shortwave and longwave diurnal signal, respectively.

Figure 18 (upper) shows the July diurnal cycle of zonal mean high cloud cover over land in the GCM (left) and ISCCP (right). The GCM results are averaged over 3-h intervals of local time to match the ISCCP temporal resolution. The GCM successfully simulates the afternoon high cloud maximum over summer midlatitude land, and the slightly later maximum over tropical land, although the observed maximum at most latitudes is 2–3 h later than the simulated peak. The GCM also correctly simulates the increase in diurnal amplitude from midlatitudes to the Tropics, although the GCM midlatitude amplitude is too weak. In January (not shown), the GCM has no clear midlatitude diurnal cycle, while ISCCP has a weak afternoon peak.

The diurnal cycle of high cloud over ocean is shown in Fig. 18 (lower). ISCCP indicates a strong semidiurnal component over midlatitudes of both hemispheres, with maxima near both dawn and dusk. In the Tropics the signal is more diurnal with the dusk maximum dominating. The GCM produces a maximum several hours before dawn at most latitudes, with a secondary maximum several hours before dusk present mostly in the subtropics and higher latitudes. Both the model and ISCCP produce very weak amplitudes (2%) for the diurnal cycle of oceanic high cloud. The GCM's tropical peak is reminiscent of that observed in most of the tropical Pacific, but several hours earlier (Fu et al. 1990). The absence of a GCM evening equatorial maximum, as is observed in the east Atlantic, may be indicative of the model's generation of propagating African easterly waves.

Figure 19 shows the corresponding diurnal cycles of total cloud cover. Except near the equator over land, where the observed diurnal cycle is controlled by the evening maximum in high cloudiness, both the model and ISCCP results are indicative of the diurnal cycle of low cloud. The GCM's diurnal cycle of continental low cloud peaks in morning, however, while that observed by ISCCP peaks generally in early afternoon. Over ocean, the GCM agrees with ISCCP's placement of the diurnal maximum of total cloud slightly before dawn. The GCM also correctly simulates the rather large diurnal amplitude over land and the small amplitude over ocean. Except over tropical land, neither the GCM nor ISCCP indicate dramatic latitudinal variation of diurnal cycle phase; the observed peak is perhaps a bit later in the morning in midlatitudes than in the Tropics.

The GCM's misplacement of the continental maximum in total cloud is its most glaring shortcoming. Surface observations of low cloud indicate the same afternoon maximum over land that ISCCP observes in total (and low) cloud (Warren et al. 1986, 1988). The surface observations contain morphological distinctions between cumulus and stratus + stratocumulus + fog. The former peaks in early to midafternoon over land, while the latter peaks in the early morning. Since the diurnal cycle of cumulus is about twice as large as that of the stratiform low cloud, the former determines diurnal cycle phase.

In the GCM, the situation is reversed. Shallow convection occurs almost as frequently (20%–30%) in the model as in the observations, except in western North America. But the cloud amount when present is only about 5%, as opposed to 25%–35% in the data. Thus, only a few percent of the GCM's 25%–30% low cloud cover over land is convective, and hence its diurnal cycle is determined by the morning peak in low stratus. Apparently the GCM is too unstable over land in early

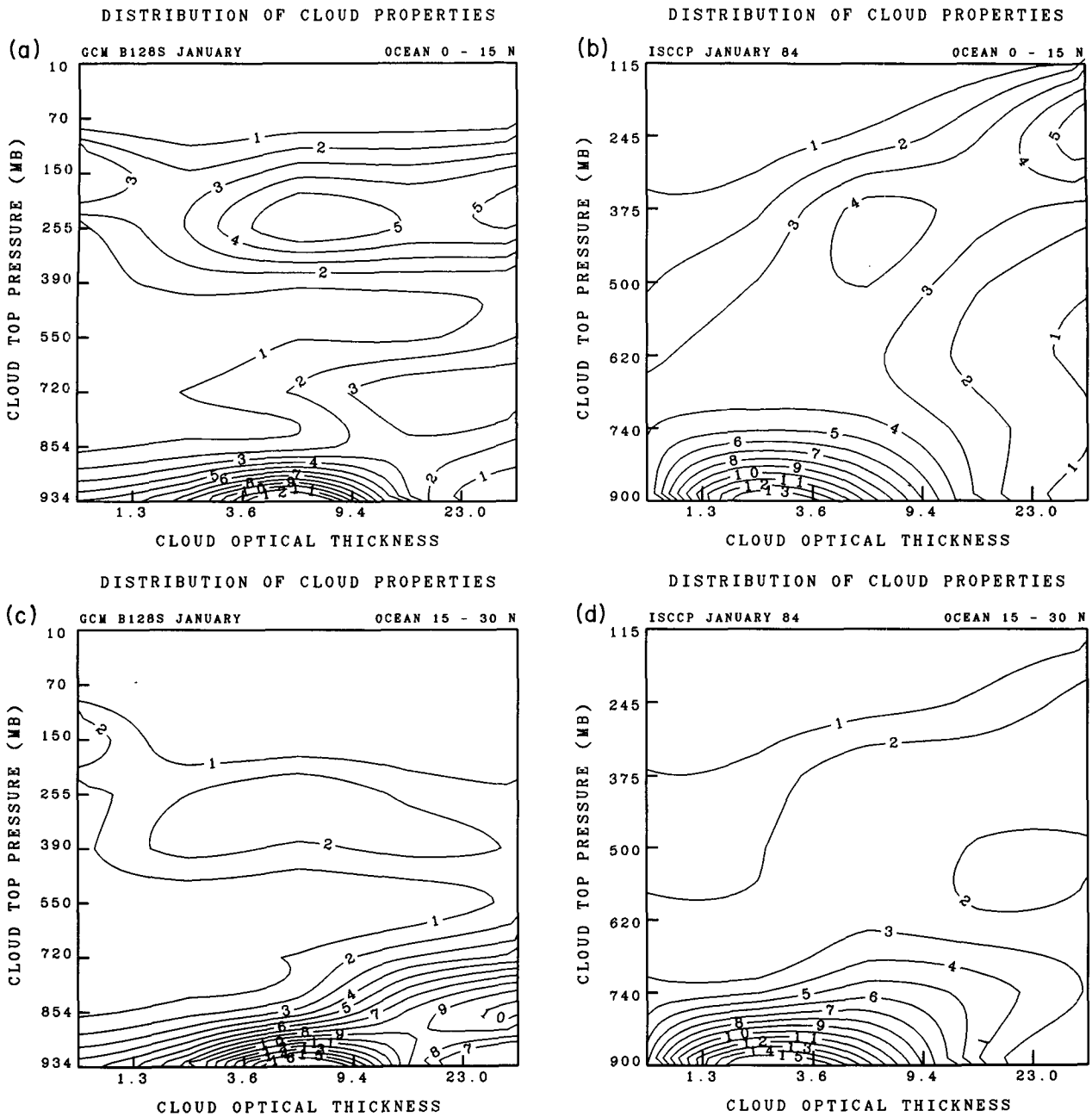

FIG. 14. Two-dimensional frequency histograms of cloud-top pressure (mb) and visible optical thickness over tropical and subtropical oceans in the GCM and ISCCP C1 data. The GCM cloud properties have been binned into the same five optical thickness ranges reported by ISCCP. The cloud-top pressure categories are different in the model and data: ISCCP reports seven cloud-top pressure categories, while the GCM figures denote the tops of the nine model levels. The GCM histograms are 5-day averages and have been subjected to the satellite "detection" procedure described in the text; the ISCCP data are averages for the full month of January 1984: (a) GCM, 0°–15°N ocean; (b) ISCCP, 0°–15°N ocean; (c) GCM, 15°–30°N ocean; (d) ISCCP, 15°–30°N ocean.

afternoon, generating deep convection when shallow fair-weather cumulus should dominate. This is a land problem only; over oceans, the GCM has fairly realistic cumulus mass flux distributions and the correct diurnal phase.

b. Seasonal cycle

The seasonal variation of cloud properties is affected by the migration of the ITCZ across the equator, the reduction in equator–pole temperature contrast in sum-

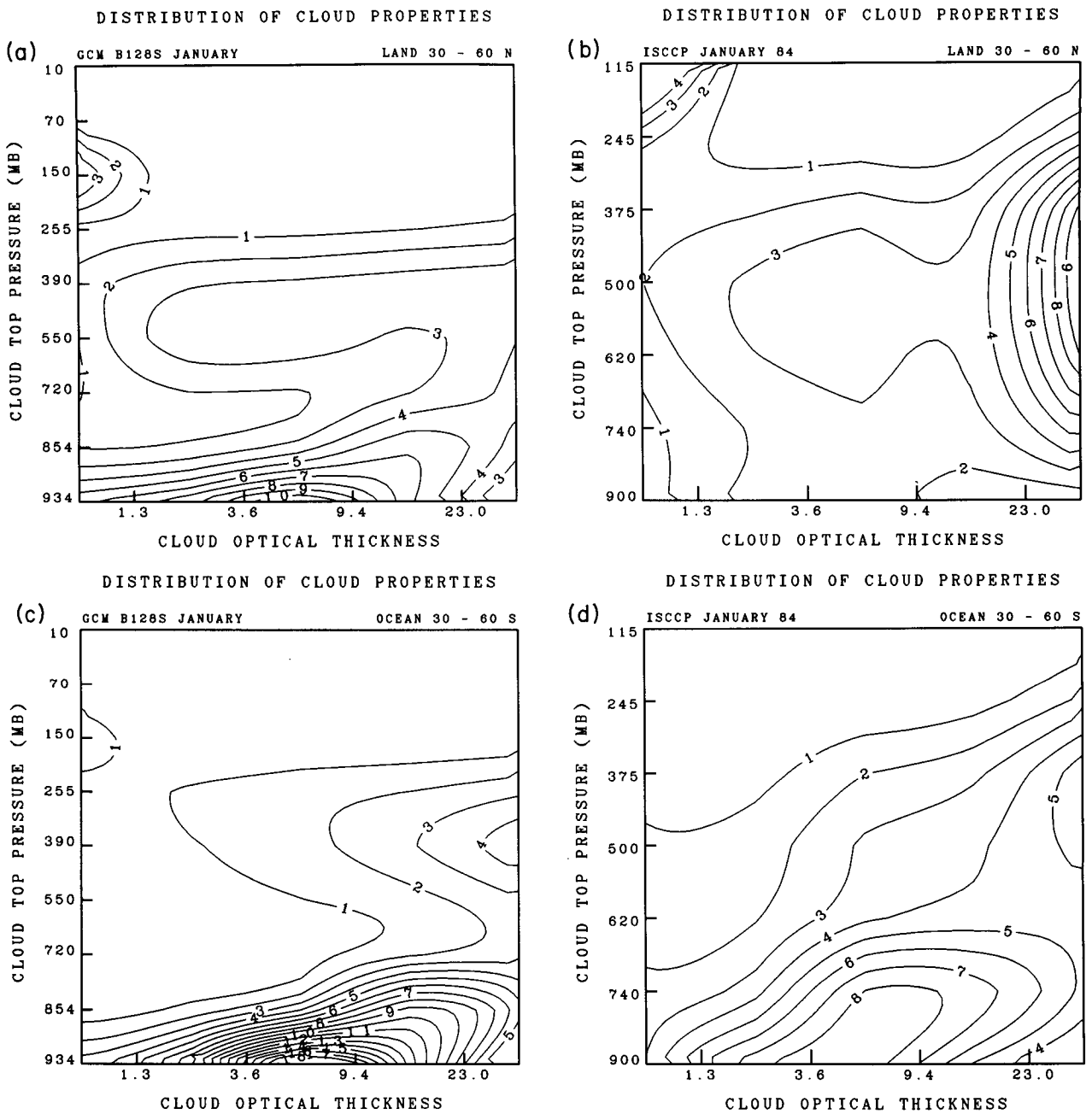

FIG. 15. As in Fig. 14 but for midlatitude land and ocean regimes: (a) GCM, 30°–60°N land; (b) ISCCP, 30°–60°N land; (c) GCM, 30°–60°S ocean; (d) ISCCP, 30°–60°S ocean.

mer and associated decline and poleward shift in baroclinic wave activity, the increase in convective instability in summer, and the seasonal melting of snow and sea ice. The first of these has no simple relationship to long-term climate change and sensitivity, hence the climatic irrelevance of hemispheric mean seasonal changes. But the others are indicative of changes predicted to occur in a warming climate, so seasonality can be a useful validation tool.

Figure 20 shows the zonal mean seasonal cycle of high cloud cover over land (upper) and ocean (lower) simulated by the GCM (left) and observed by ISCCP (right). Over both land and ocean, the dominant feature is the movement of the ITCZ, which lags insolation by 1 month over land and 2 months over ocean in both data and model. The GCM seasonal amplitude is about twice as strong over land as over ocean, somewhat more than the observed land–ocean difference. The maximum sea-

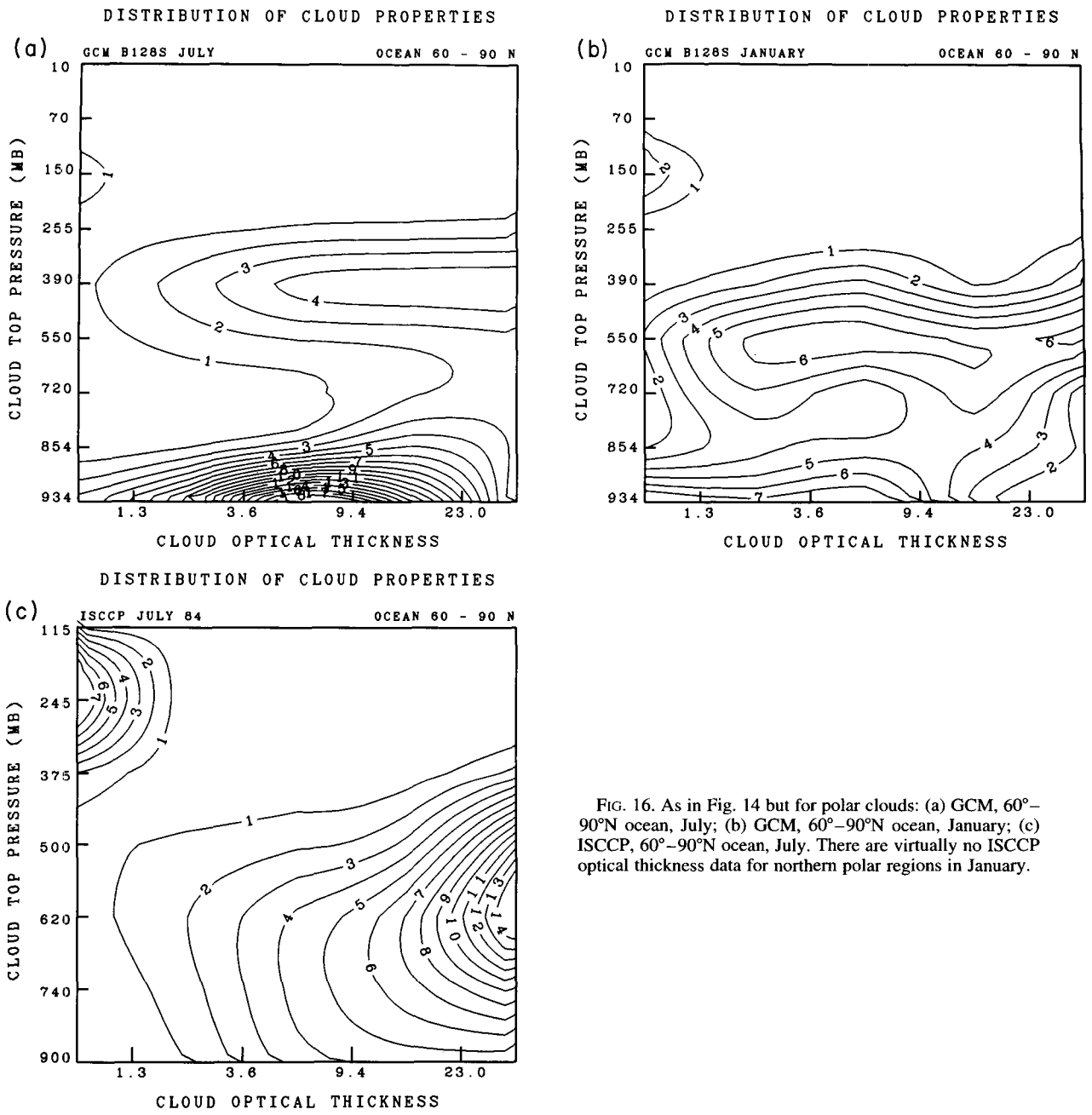

FIG. 16. As in Fig. 14 but for polar clouds: (a) GCM, 60°–90°N ocean, July; (b) GCM, 60°–90°N ocean, January; (c) ISCCP, 60°–90°N ocean, July. There are virtually no ISCCP optical thickness data for northern polar regions in January.

sonal excursion is correctly simulated to be 10°–20° lat in summer over land, but over ocean the GCM's ITCZ drifts poleward to 20°–25°, while the observed ITCZ remains within 10°–15° of the equator.

Of more interest climatically is midlatitude high cloud cover, which is plausibly an index of deep convection. Both the GCM and ISCCP produce a continental peak in late summer at high latitudes which shifts toward spring in midlatitudes, with amplitudes less than half that of the ITCZ migration. ISCCP's midlatitude peak is actually in late winter, while the GCM's is several months later. This is consistent with the GCM's winter dry bias. Over ocean there is a weaker seasonal amplitude of high cloud in both model and observations, with the GCM's peak occurring in midsummer, while ISCCP shows a summer peak at high latitudes but a semiannual structure with late summer and early winter peaks in midlatitudes.

Figure 21 shows the corresponding seasonality in total cloud cover. In the Tropics, the seasonal cycle of total cloud is dominated by high cloudiness, and is thus similar to that in Fig. 20. In middle and high latitudes,

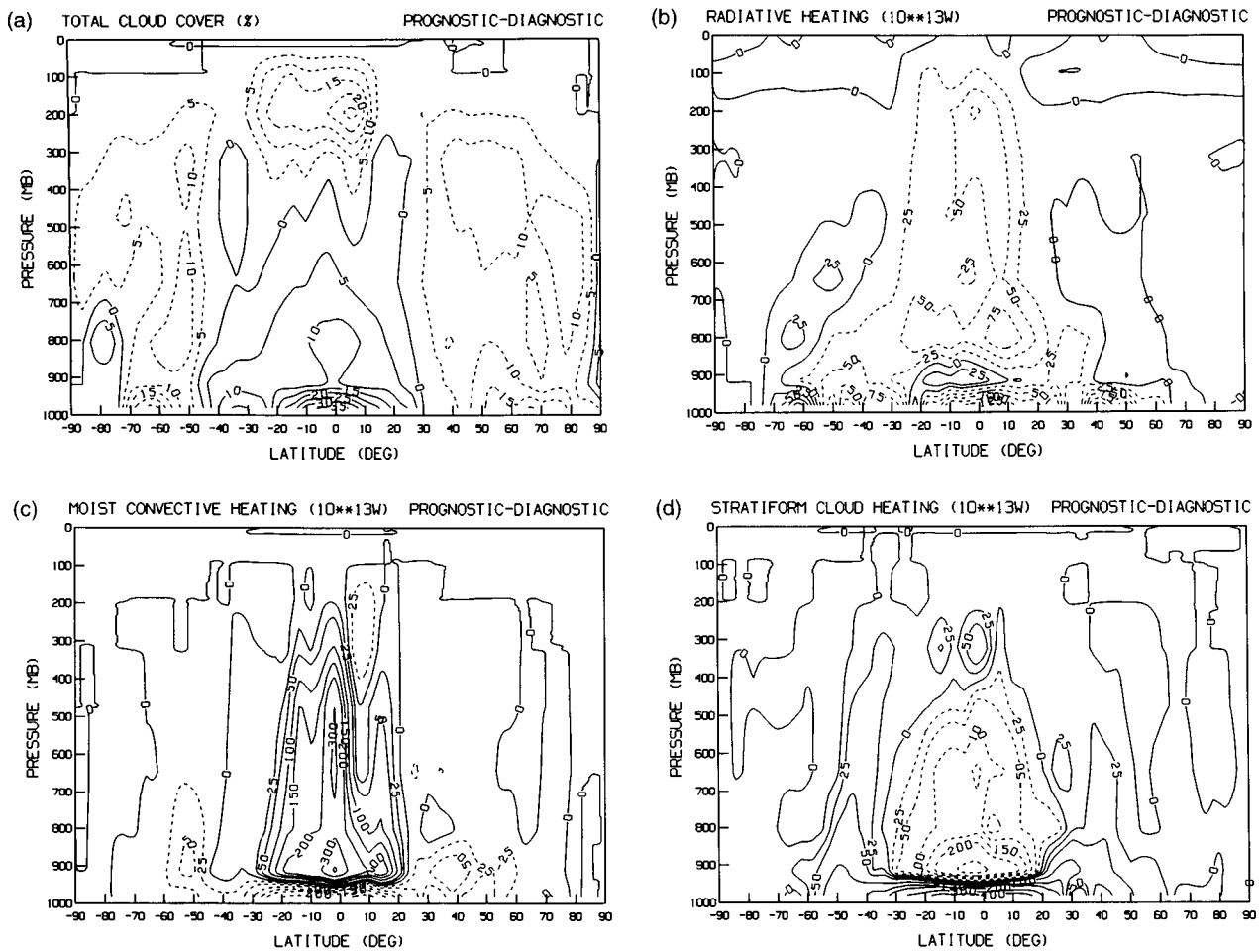

FIG. 17. Zonal mean January differences between the control run with the new prognostic cloud water parameterization and a sensitivity experiment using the GISS Model II diagnostic cloud parameterization: (a) Total cloud cover (%); (b) total radiative heating rate (10^{13} W); (c) moist convective heating rate (10^{13} W); (d) stratiform condensation heating rate (10^{13} W).

low cloud contributes to the seasonal cycle but more so in the model than in the data. Over ocean both model and data indicate a broad maximum of total cloudiness in late fall and winter in the Northern Hemisphere and late winter into spring in the Southern Hemisphere, but weaker in the model, consistent with its deficient baroclinic wave activity. There is also a weak secondary northern midlatitude peak in summer. Over land, the GCM disagrees with ISCCP in the following several ways: 1) Due to the model's excessive Siberian winter cloud cover (cf. Fig. 10), its seasonal cycle in northern midlatitudes is completely out of phase with the observations at 50°–60°N, and several months out of phase at 30°–50°N. 2) In southern midlatitudes, the model's total cloud peaks in winter while ISCCP has a semiannual behavior with an additional late spring peak. 3) In the GCM, polar cloudiness peaks in summer in both hemispheres while ISCCP indicates a winter peak; here ISCCP disagrees with surface climatologies and may be in error (Mokhov and Schlesinger 1994), although "cloudless" ice crystal precipitation unaccounted for in some datasets complicates the interpretation (Curry and Ebert 1992).

Seasonal variations in cloud forcing will be documented elsewhere as part of the FANGIO (Feedback Analysis of GCMs and Intercomparison with Observations; cf. Cess et al. 1990) GCM intercomparison activities. Here we only briefly note the major features of the model-ERBE seasonal comparison. For comparison purposes, ERBE zonal mean, area-weighted seasonal changes were defined as January minus July and Southern Hemisphere minus Northern Hemisphere; the result is effectively a composite summer minus winter change at each latitude. Relative to the ERBE standard, the GCM's rms cloud forcing differences are 13.7 (C_s) and 12.4 (C_l) W m^{-2}, and the correlation coefficients between the GCM's and ERBE's seasonal variations are 0.88 (C_s) and 0.94 (C_l). The sources of the differences are readily determined by examining Figs. 7–13 and 20–21. In the Tropics over ocean, where the ITCZ

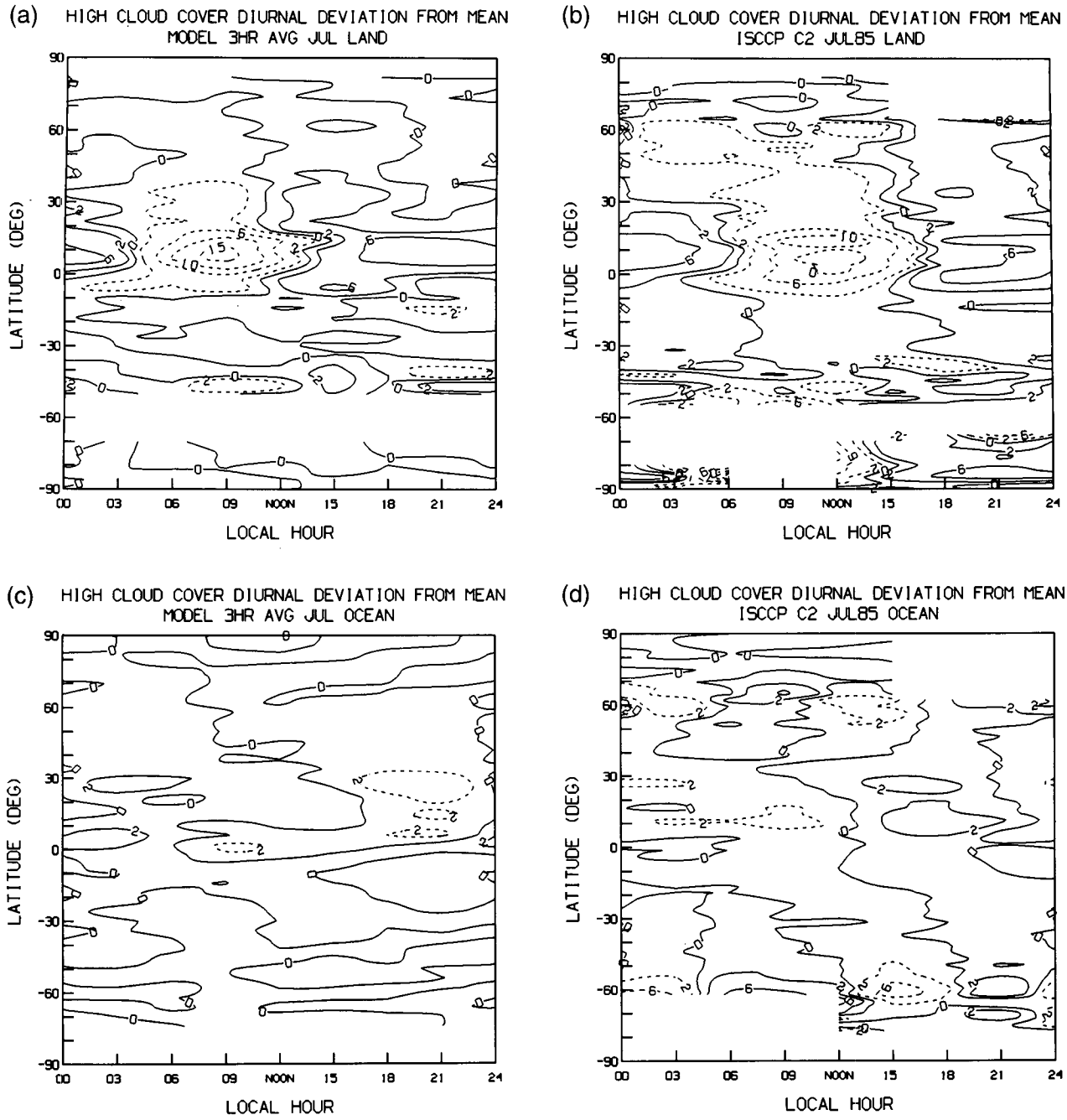

FIG. 18. Diurnal cycle of July high cloud cover (deviation from the zonal, monthly, and daily average) as a function of latitude and local hour for a single month of the GCM and ISCCP C2 data. The ISCCP estimate uses the IR detection threshold only: (a) GCM, land; (b) ISCCP, land; (c) GCM, ocean; (d) ISCCP, ocean. Units: (%).

shifts too far poleward in summer, the GCM produces 15–20 W m^{-2} positive/negative C_s errors at 10°/20° lat, and comparable errors of opposite sign in C_l. In midlatitudes, underestimates of storm track cloudiness and cloud liquid water content cause the GCM to underestimate the seasonal variation of cloud forcing by a similar amount. At higher latitudes, the GCM's excessive low cloudiness over Eurasia in winter and deficit in summer produce a 20 W m^{-2} error in C_s but almost no error in C_l.

c. *Interannual variations*

Figure 22 shows Hovmöller diagrams of OLR and precipitation anomalies at the equator across the Pacific

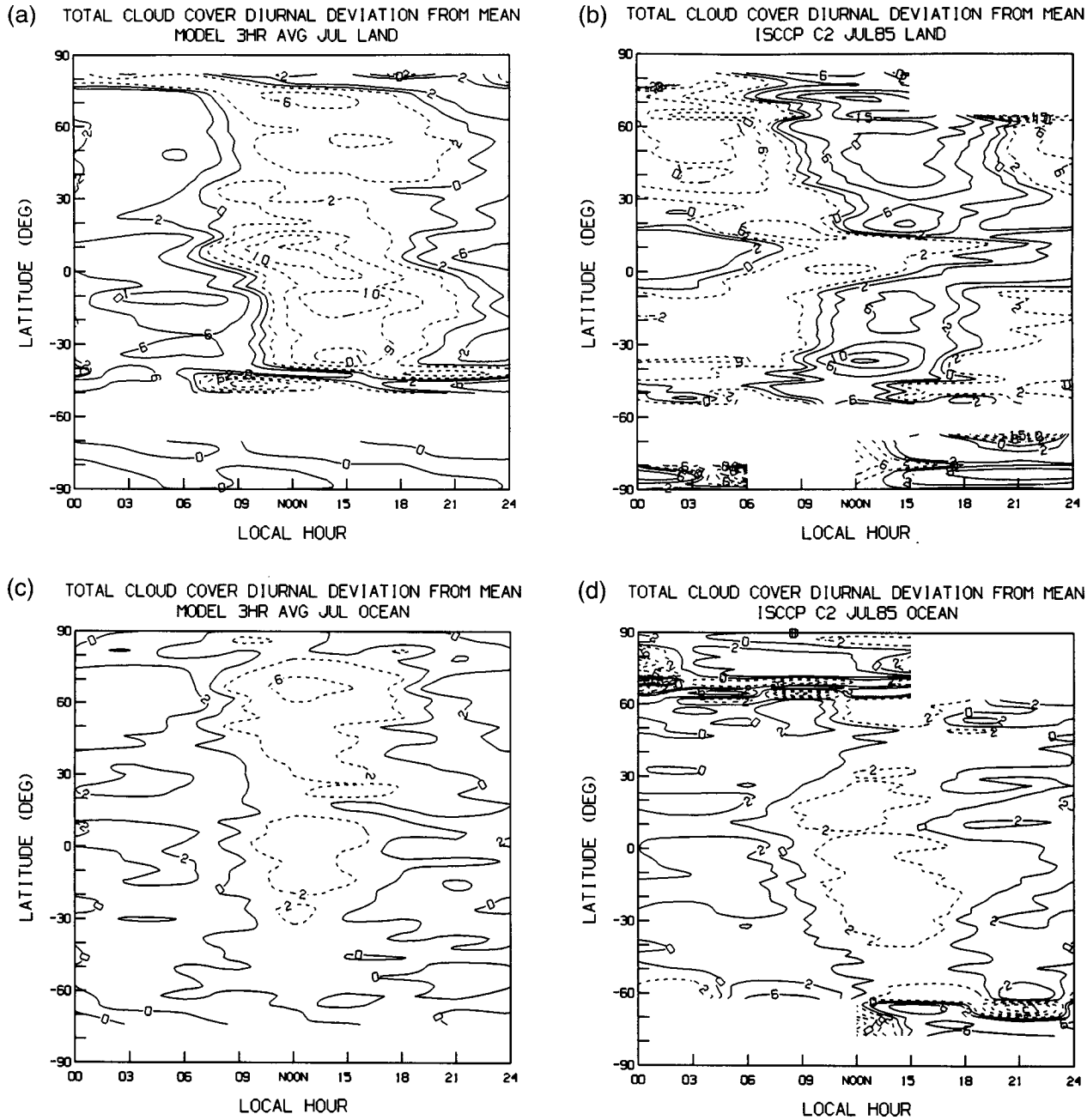

FIG. 19. As in Fig. 18 but for total cloud cover.

for 1979–1988, with the GCM forced by observed AMIP SSTs. Compared to observations (Kousky and Leetmaa 1989), the simulation of OLR anomalies for the 1987 El Niño–Southern Oscillation (ENSO) is quite good. Both model and data suggest peak anomalies of >40 W m^{-2} in early 1987 just east of the dateline; the GCM's peak is about 10° east of the observed peak and persists further into the year. Prior to the El Niño, both model and data show negative anomalies in the central Pacific of 10–30 W m^{-2} and slightly smaller positive anomalies in the west; the peak negative anomaly occurs just west of the date line in winter 1984, precisely as observed. The model representation of the 1982/83 ENSO is not quite as good but acceptable: the maximum OLR anomaly is about 40 W m^{-2} vs 60 W m^{-2} observed and is spread over the central and east Pacific rather than focused near 150°W. The corresponding precipitation anomaly record in Fig. 22,

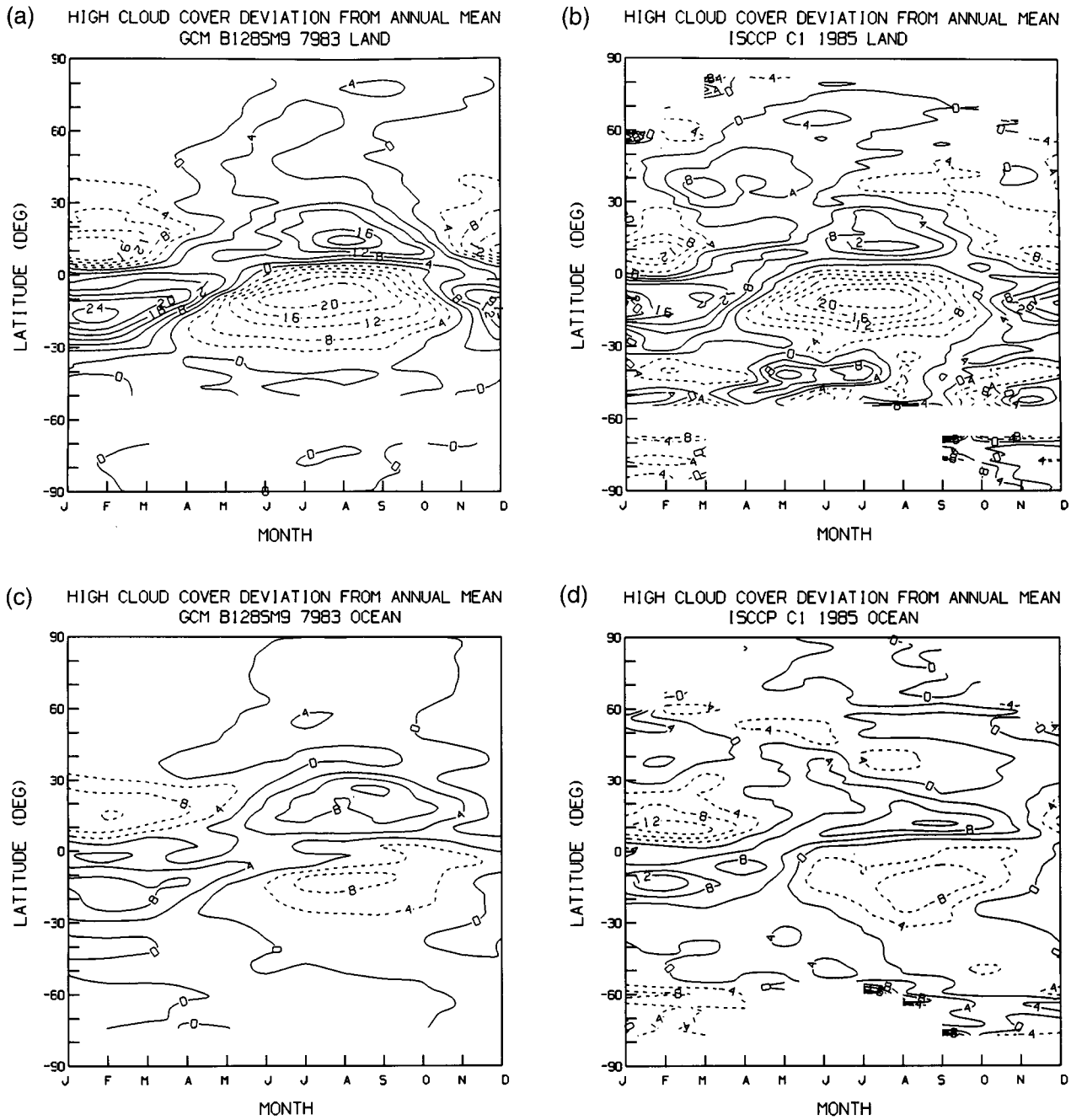

FIG. 20. As in Fig. 18 but for the seasonal cycle of high cloud cover (deviation from the zonal, annual mean) as a function of latitude and month. The ISCCP estimate uses daytime data only and a combined visible–IR detection threshold.

though having no reliable observational counterpart, matches most of the features of the OLR record, suggesting that ENSO OLR anomalies are caused by the optically thick anvil clouds accompanying deep precipitating convective systems. Anomalies in low-level wind fields (not shown) are also realistic, suggesting that the GCM produces the correct dynamic response.

Ramanathan and Collins (1991) have examined interannual differences in ERBE TOA shortwave and longwave cloud forcing in the tropical Pacific. The corresponding GCM simulation of the correlation between C_s and C_l differences between ENSO and non-ENSO months is shown in Fig. 23. Diagrams such as these simply reflect dynamical shifts in locations of extensive

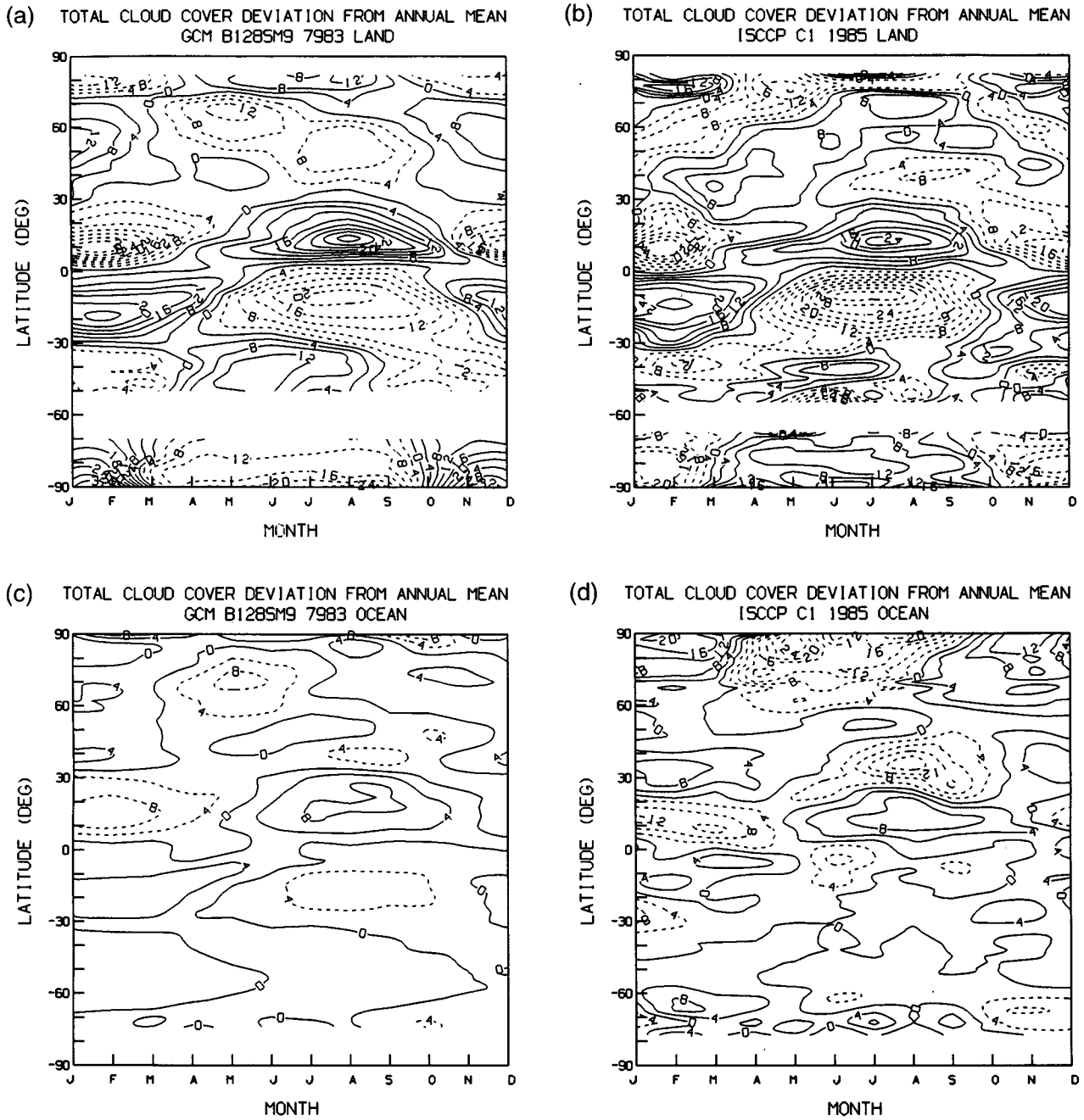

FIG. 21. As in Fig. 20 but for total cloud cover. The ISCCP estimate uses the visible–IR threshold for daytime data and the IR-only threshold for nighttime data.

deep convection and thus contain no information about the presence or absence of "thermostat"-type feedbacks on SST change (Fu et al. 1992). Nonetheless, the data provide a useful test of the model's ability to simulate cloud radiative properties; in particular, since longwave and shortwave perturbations are highly correlated, Fig. 23 is an indicator of the GCM's success in simulating cumulus anvils. The GCM does an excellent job in reproducing the ERBE results, with C_s differences of up to about ± 70 W m^{-2} and C_l differences of up to ± 50 W m^{-2}; the slope of the best fit is -1.14, almost identical to the -1.20 seen by ERBE. This result may be somewhat fortuitous, given the GCM's simplistic prescription for detrainment of convective condensate and its use of Mie scattering for ice clouds (see section 6). Surface shortwave cloud forc-

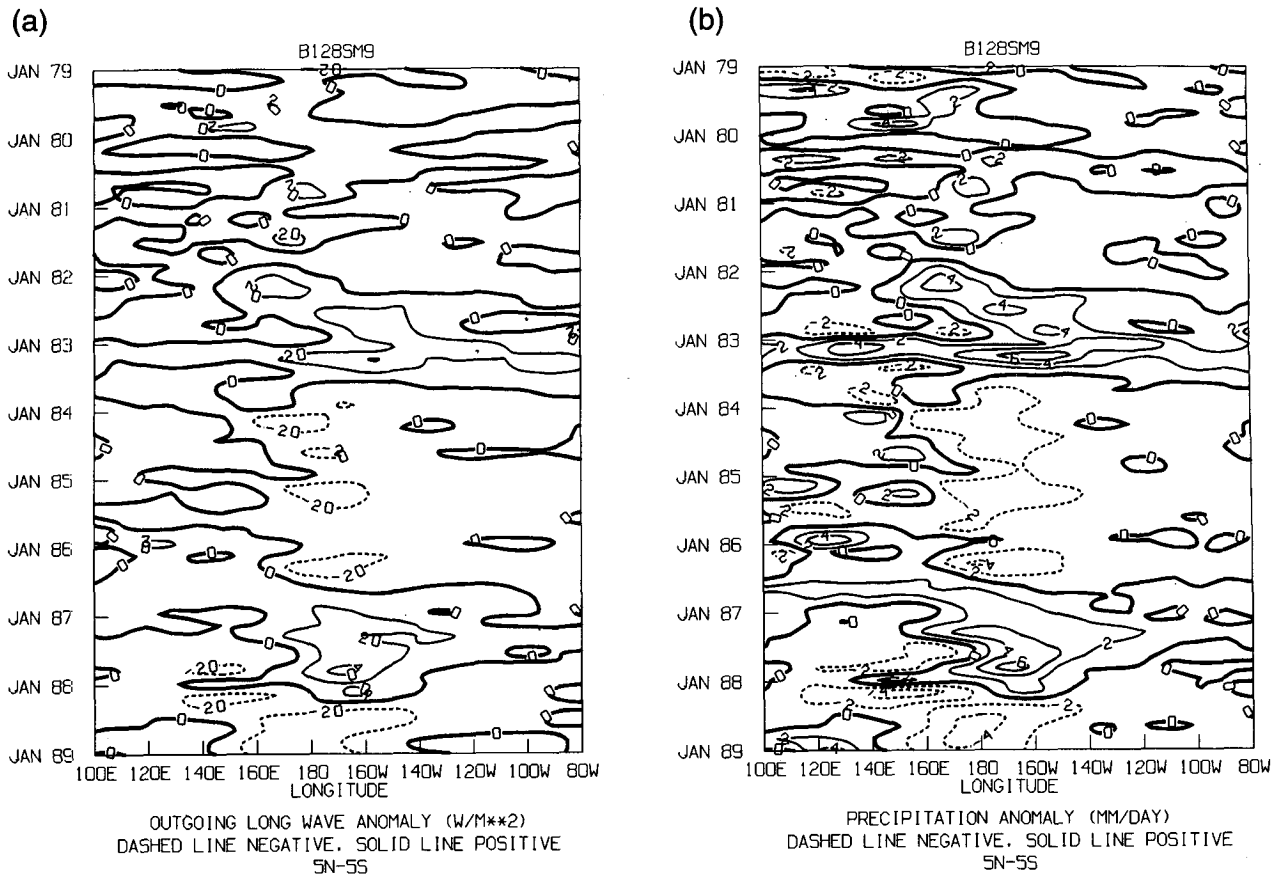

FIG. 22. Hovmöller diagrams of equatorial (5°S–5°N mean) Pacific (a) OLR and (b) precipitation anomalies relative to the 1979–1988 mean, smoothed to 8° × 10° resolution, simulated by the GCM forced with AMIP SSTs. OLR is defined here to be a negative quantity (cf. Table 1); positive anomalies denote less radiation emitted to space.

ing in the GCM (not shown) is almost identical to TOA shortwave forcing, with small (<5 W m^{-2}) systematic differences of opposite sign for gridboxes dominated by high and low clouds. Surface longwave cloud forcing (not shown) is small (10–15 W m^{-2}) throughout the tropical Pacific and weakly negatively correlated with shortwave forcing; the small magnitude is realistic given the large specific humidity of the tropical PBL.

5. Temperature dependence and sensitivity

Increasingly, variability of climate parameters is being analyzed as a function of temperature variations in the current climate under the (sometimes implicit) assumption that such correlations are interpretable as a climate feedback. But the observed variability is as likely to be produced by variations in the dynamics as by intrinsic temperature dependence; in most cases the dynamic and thermodynamic influences have not yet been separated. Nonetheless, observed temperature dependence, whatever its cause, presents another test for cloud parameterizations. Comparison of such behavior for the current climate with actual simulations of the GCM response to temperature perturbations is a first step in unraveling the dynamic and thermodynamic contributions to cloud variability.

A major unsolved problem in climate is the temperature dependence of cloud optical thickness. In situ data (Feigelson 1978) and adiabatic liquid water behavior (Betts and Harshvardhan 1987) suggest that cloud liquid water content, and by inference optical thickness, should increase monotonically with temperature. Tselioudis et al. (1992) found, however, that low clouds in the ISCCP dataset exhibit this behavior only at cold temperatures, and more so over land than ocean. Elsewhere, τ decreases with temperature instead. Figure 24 shows the simulated temperature variation of low cloud optical thickness for individual GCM layers over ocean. At cold temperatures, τ increases with T; for $T > 10$°C, τ decreases with T instead, except at the very warmest temperatures. Sensitivity tests indicate that parameterized vertically subgrid-scale cloud physical thickness variations [Eqs. (9) and (25)] are responsible for this behavior. Figure 24 applies to individual

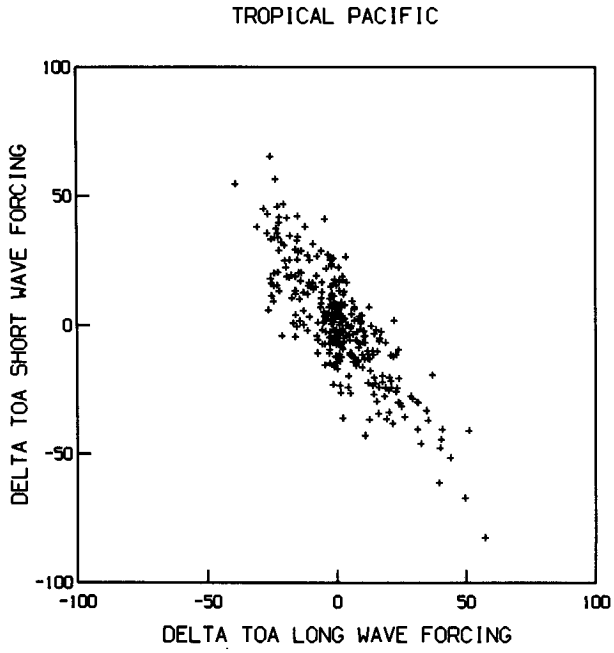

FIG. 23. April 1987 minus April 1985 and February 1988 minus February 1987 differences in C_s vs C_l for tropical Pacific (10°S–10°N, 124°E–90°W) gridboxes simulated by the GCM forced with the AMIP SSTs.

layer optical thicknesses; when total column τ is computed for low clouds with no higher clouds overhead, analogous to the view from satellite, the change from positive to negative $d(\ln\tau)/dT$ occurs near 0°C, and both the change in this quantity with latitude and the difference in land vs ocean behavior agree fairly well with ISCCP inferences.

Ice water content for high clouds in the GCM (Fig. 25) increases with T until leveling off for $T > -25$°C, where the liquid phase starts to become significant. The rate of increase with temperature is fairly consistent with in situ ice water content measurements (Heymsfield and Donner 1990), although the data vary considerably from one region and synoptic situation to another. The Heymsfield and Donner data correspond to cirrus clouds rather than cumulus anvils. For comparison, we separate high clouds in Fig. 25 into convective and nonconvective situations. GCM "anvils" tend to have systematically higher ice water contents than other high clouds, since they have an ice water source from cumulus detrainment, but their temperature dependence is not markedly different. High anvil ice water contents (0.1–0.3 g m^{-3}) are typical of the limited available observations as well (Griffith et al. 1980; Churchill and Houze 1984).

It is not clear a priori whether such correlations are indicative of feedbacks that would occur in a climate change. As one hypothetical example of a climate change, the FANGIO intercomparison project analyzes GCM response to imposed globally uniform ±2°C changes in SST under perpetual July conditions with fixed sea ice and soil moisture. The climate sensitivity in such experiments is defined as $\lambda = (\Delta F/\Delta T_s - \Delta Q/\Delta T_s)^{-1}$, where ΔT_s is the global mean surface temperature difference between the +2°C and −2°C realizations and ΔF and ΔQ are the corresponding changes in OLR and ASR, respectively, forced by the imposed climate change; by calculating the sensitivity separately for clear skies (λ_c), cloud feedback can be estimated as λ/λ_c (cf. Cess et al. 1990).

Table 3 compares the sensitivity and feedback contributions for the prognostic cloud water budget parameterization with those for Model II. The new version of the GCM calculates clear sky quantities at each gridbox while the old version used clear gridboxes only, but the effects on sensitivity and feedback are unimportant. Optical thickness in Model II is prescribed to decrease with height. As a result, F increases with T_s by similar amounts in clear and cloudy regions, because an increase in cloud height (which reduces OLR) in the warmer climate is accompanied by both a decrease in total cloud cover (mostly due to low and middle clouds) and an implicit decrease in column optical thickness (which increases OLR). Q increases dramatically with T_s because cloud cover and optical thickness decrease. The solar effect dominates, producing a large climate sensitivity and strongly positive cloud feedback ($\lambda/\lambda_c \gg 1$).

The prognostic scheme behaves quite differently. Cloud cover now slightly increases with warming, and while cloud height still increases, a local increase in optical thickness at many model levels more than com-

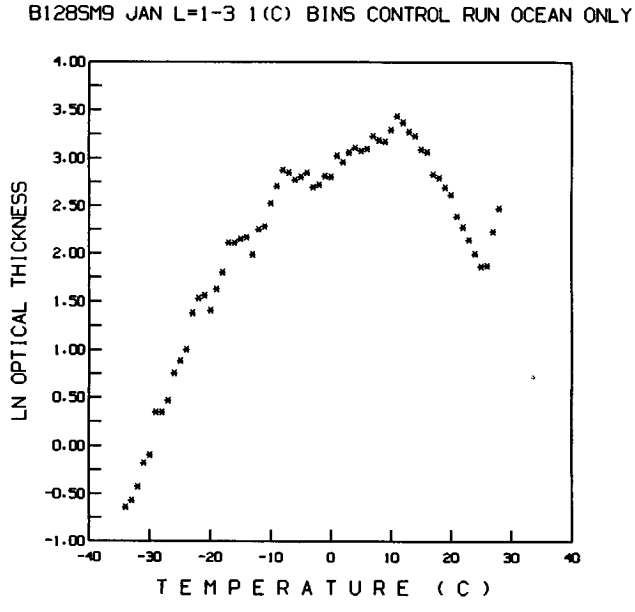

FIG. 24. Logarithm of cloud optical thickness for individual GCM layers for low-level clouds over ocean vs layer temperature (°C), binned into 1°C intervals, for January.

pensates the effect of the upward shift. Thus, in the new model there is more of an enhanced greenhouse effect (smaller $\Delta F/\Delta T_s$) in the warmer climate, but a decrease in solar absorption (negative $\Delta Q/\Delta T_s$). The latter dominates, producing a very low climate sensitivity and negative cloud feedback ($\lambda/\lambda_c < 1$).

To understand the lower sensitivity of the new parameterization, consider the zonal mean changes in cloud cover and cloud water content (Fig. 26). High cloud cover increases, especially in the Tropics, in the warmer climate, but unlike the first generation of GCMs with diagnostic cloud schemes, cloud cover does not uniformly decrease with temperature outside the polar regions below the tropopause. Instead, a complex pattern of cloud cover changes results, with at least the following two probable causes: 1) Cloud cover increases near the low-latitude trade inversion (700–800 mb); this may represent increased venting of boundary layer moisture by shallow cumulus. 2) Above this level, cloudiness decreases, primarily just above the 0°C isotherm. This is suggestive of the increase in autoconversion produced by the Bergeron–Findeisen process (see Fig. 1), which decreases the lifetime of mixed phase clouds; as T_s increases, the level at which this process operates preferentially shifts upward and high-altitude ice production increases, causing a local cloud cover decrease. This is a direct result of the use of a prognostic cloud water parameterization. Note, however, that prognostic schemes that neglect the Bergeron process produce a midlevel cloud cover increase with warming instead (Senior and Mitchell 1993), and thus a low sensitivity.

Cloud water content changes with warming generally mirror the pattern of cloud cover changes, but the magnitude of the change is greatest in the tropical cumulus anvil region and not coincident with the location of largest cloud cover change. This suggests that climate changes in anvil microphysical properties are primarily responsible for the negative cloud feedback and low sensitivity of this version of the GCM. By comparison, low-level cloud water changes are small and roughly coincident with changes in cloud cover, suggesting that the in-cloud water content response to the climate change is modest.

The extreme sensitivity of the GCM to high cloud feedbacks raises two questions. First, since the GCM is deficient in midlatitude cirrus (Fig. 11), does it un-

TABLE 3. TOA radiation balance and cloud-forcing differences (W m^{-2}), climate sensitivity [°C/(W m^{-2})], and cloud feedback produced by the diagnostic cloud parameterization run in the previous Model II GISS GCM and by three different versions of the prognostic cloud water parameterization run in the new GISS GCM under perpetual July conditions with fixed sea ice and soil moisture and subjected to +2°C and −2°C SST perturbations.

	Model II	Prognostic cloud water	Enhanced high cloud	Reduced SST gradient
ΔQ				
clear	0.00	0.51	0.57	0.52
total	4.88	−1.28	−1.09	0.48
ΔC_s	4.88	−1.79	−1.66	−0.04
ΔF				
clear	7.72	7.73	8.12	5.62
total	8.16	6.89	7.24	3.86
ΔC_l	−0.44	0.84	0.88	1.76
λ	1.23	0.49	0.49	1.12
λ/λ_c	2.37	0.88	0.91	1.51

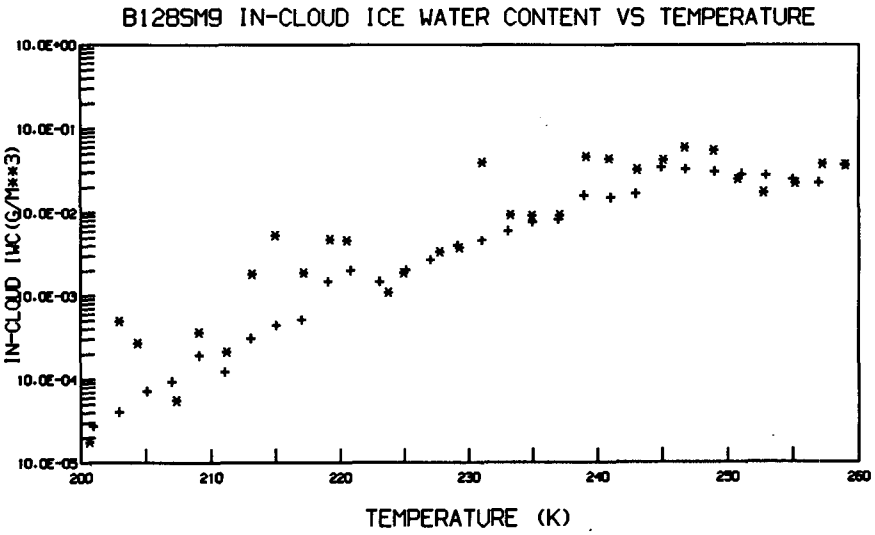

FIG. 25. In-cloud ice water content (g m^{-3}) for individual GCM layers for high-level clouds vs layer temperature (°C), binned into 1°C intervals, for a 24-h period in January. Asterisks denote cumulus anvils and plus signs denote other cirrus not associated with deep convection.

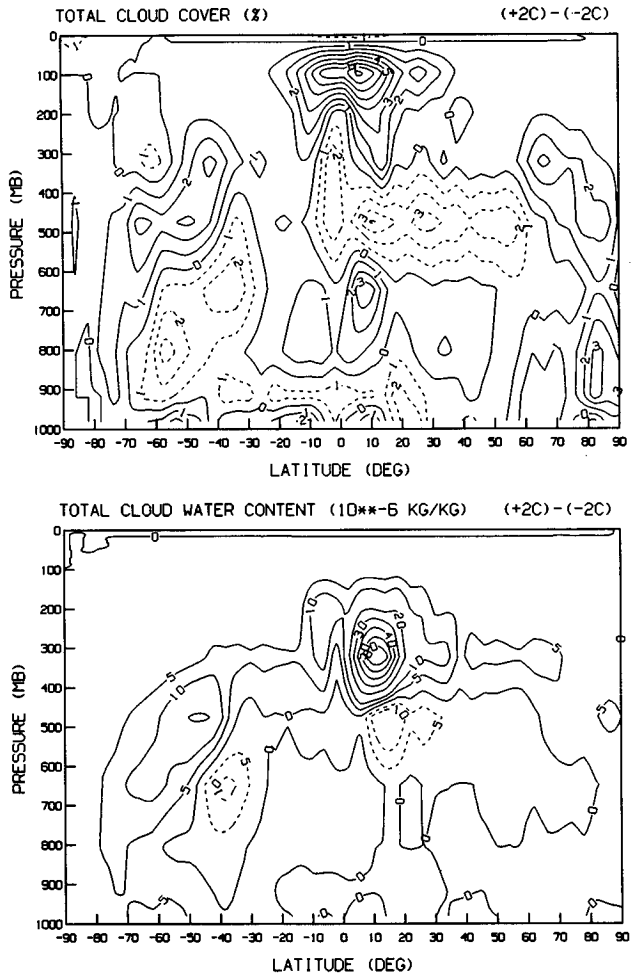

FIG. 26. Difference in zonal mean total cloud cover (%) and cloud water content (10^{-6} kg kg^{-1}) between GCM perpetual July runs with prescribed globally uniform +2°C and −2°C perturbations in SST.

derestimate sensitivity by underestimating climate changes in the greenhouse effect of these clouds? To test this proposition, we performed an experiment in which high cloud cover was artificially enhanced outside the Tropics by allowing U_{00} to decrease from 0.6 at the equator to 0.25 at the pole for ice clouds. The parameterization change roughly doubles midlatitude high cloud cover and increases C_l by 5 W m^{-2} globally in the current climate. But as Table 3 indicates, the change has virtually no effect on climate sensitivity. There are two reasons for this: 1) comparable decreases in C_s in the current climate offset the longwave changes; 2) although the mean C_l is different in the two experiments, the climate change ΔC_l is almost identical. This is evidence of our earlier assertion that validation of the mean state by itself contains no information about a GCM's response to perturbations.

The results of this experiment reinforce the notion from Fig. 26 that it is the tropical anvil clouds that matter most to climate sensitivity. This raises a second question: Does Fig. 26 argue for the concept of a tropical cirrus "thermostat" that limits long-term climate change? Unfortunately, the prescribed SST climate change is a poor proxy for greenhouse gas–induced climate change, which may involve changes in SST patterns as well. To explore the effect of such differences, we performed a final experiment in which SST changes were applied uniformly only outside the tropical Pacific. Within the tropical Pacific, SST changes were prescribed so as to average ±2°C in the longitudinal mean, but with the temperature change greatest in the coldest regions (Ye et al. 1995). This drastically reduces the zonal SST gradient in the warmer climate (to about 2°C across the Pacific) while increasing the gradient in the cooler climate. There are several reasons to anticipate such behavior at least qualitatively in an actual climate change. 1) The east Pacific Ocean mixed layer is shallower than its western counterpart and thus responds more quickly to perturbations. 2) The thermostat concept, if valid, would require the convective west Pacific to respond less to a perturbation than the mostly nonconvective east Pacific.

The reduced SST gradient weakens the Walker circulation in the warmer climate. The moisture convergence source of anvil cloud water in the west Pacific is therefore reduced relative to the uniform SST change case, and changes in the east are not sufficient to compensate. Table 3 shows that this experiment, despite identical physics to the standard prognostic version, produces a distinct positive cloud feedback and fairly large climate sensitivity instead, the biggest change being the virtual elimination of negative shortwave impacts in association with warming. Of course, this is still a prescribed SST change experiment; in a real climate change, the SST pattern, Walker cell, and anvil clouds will interact to produce an equilibrium change that may differ from either of the two extremes we have examined here. But the results of these tests demonstrate two important points. 1) Climate sensitivity to greenhouse gas increases can be determined only in the context of actual climate change scenarios with coupled atmosphere–ocean models. 2) The thermostat concept is too simplistic to apply to global climate change, since tropical anvil properties depend on the general circulation and thus the SST gradient rather than merely responding to local changes in SST.

6. Discussion

Our experiments indicate that realistic simulation of tropical cumulus anvil radiative properties and their variation is crucial for a plausible climate sensitivity estimate. The GCM reproduces observed shortwave and longwave cloud forcing variations over ENSO, but we use equivalent spheres to calculate ice-scattering properties, and realistic ice phase functions produce higher reflectances (Minnis et al. 1993). Thus, our sim-

ple prescription of anvil condensate detrainment from cumulus updrafts is likely to be an overestimate. Most observations of high clouds pertain to thin cirrus in nonconvective environments; there is a clear need for more in situ data from thick, active cumulus anvils, including ice water content, precipitation, crystal size, and TOA reflectance. There is also a need for remote-sensing techniques capable of determining the global distribution of ice water content. Potential parameterization improvements include more realistic ice phase functions, relating the fraction of cumulus condensate detrained to some measure of instability, and the effect of mesoscale vertical velocities on anvil properties (cf. Heymsfield and Donner 1990). Statistics from cumulus ensemble models may be helpful in obtaining the needed information. Microphysically, it is not known whether anvils are simply high water content extrapolations of thinner cirrus, or whether completely different parameterizations are required for anvils and other high clouds.

The GCM's climate sensitivity seems to depend less on changes in low clouds, but in part that may be a result of the parameterization's ability to produce both increases and decreases of optical thickness with temperature in different climate regimes. The regional nature of this behavior suggests that at least regional climate response may be sensitive to low cloud optical thickness changes in an actual climate change, while errors in the current climate in mean low cloudiness may produce climate drift in a coupled ocean–atmosphere model. The GISS GCM's current vertical resolution (50-mb thickness of the lowest layer) is clearly inadequate to resolve potentially important PBL cloud processes, such as detachment of the boundary layer from the surface by drizzle evaporation and solar absorption and cumulus–stratocumulus interactions. However, what is really needed is an understanding of the relative importance of these processes and CTEI, and in the latter case, a better understanding of the instability process itself. Our model suggests that optical thickness variations of low clouds are determined primarily by physical thickness variations, at least at warm temperatures; in situ data from field experiments such as ARM and FIRE may shed light on this important result. Over land, errors in low cloudiness are primarily due to underestimates of shallow cumulus mass flux and the cloud cover per unit mass flux. The radiative properties of cumulus are usually an afterthought in GCMs, because deep cumulus occupy such a small area of the globe. The same is not true of shallow cumulus, though; more attention needs to be paid to predicting the areal coverage of these clouds.

The cloud types mentioned thus far have already received considerable attention from theoreticians, climate modelers, and observationalists. Midlatitude storm clouds have been greatly ignored by comparison, because the study of midlatitude storms is driven by weather prediction rather than climatic considerations. The GISS GCM has known deficiencies in its ability to simulate the dynamics of midlatitude baroclinic waves, so our parameterization may perform poorly due to incorrect dynamical forcing. But given the paucity of observations of the microphysical and radiative properties of these clouds, evaluation of the parameterization itself is virtually impossible. An important question is whether ice crystals in stratus and nimbostratus in cold seasons need to be parameterized differently from their high cirrus and cumulus anvil counterparts.

Polar cloudiness is currently so poorly observed that any climatological information would be a significant improvement. First-order issues include the need to resolve the disagreement between satellite and surface climatologies over the sense of the seasonal cycle, and confirmation of the dominant cloud types in each season. The role of these clouds in the polar surface energy budget and sea ice–albedo feedback is obviously an important consideration for any GCM that attempts to simulate climate change.

A physical basis for predicting cloud cover as a function of subgrid-scale variations in climate parameters rather than as a simple function of relative humidity is needed for all parameterizations, whether diagnostic or prognostic. The prognostic approach to parameterization is not yet preferable to the use of prescribed cloud properties if the goal is simply simulation of the mean state of the current climate, because the prognostic approach creates additional degrees of freedom and feedbacks between different parts of the system not present when fixed properties are used. This is analogous to the statement that coupled atmosphere–ocean GCMs do not yet simulate the current climate better than atmospheric GCMs bounded by prescribed SSTs. But if the goal is to predict change on any timescale, then only the prognostic approach is satisfactory, since it alone attempts to simulate the *physics* of change. The performance of our parameterization relative to diagnostic and prescribed cloud property schemes is favorable enough to conclude that prognostic cloud water should be a feature of all future climate GCMs.

Acknowledgments. We thank Alison Walker and Yuanchong Zhang for assistance with various datasets used for validation. This work was supported by the NASA Climate Program, the Tropical Rainfall Measuring Mission, and the DOE Atmospheric Radiation Measurement Program.

REFERENCES

Barkstrom, B. R., 1984: The Earth Radiation Budget Experiment (ERBE). *Bull. Amer. Meteor. Soc.*, **67,** 1170–1185.

Betts, A. K., and Harshvardhan, 1987: Thermodynamic constraint on the cloud liquid water feedback in climate models. *J. Geophys. Res.*, **92,** 8483–8485.

——, and R. Boers, 1990: A cloudiness transition in a marine boundary layer. *J. Atmos. Sci.*, **47,** 1480–1497.

Cess, R. D., and Coauthors, 1990: Intercomparison and interpretation of climate feedback processes in 19 atmospheric general circulation models. *J. Geophys. Res.*, **95,** 16 601–16 615.

Churchill, D. D., and R. A. Houze Jr., 1984: Mesoscale updraft magnitude and cloud-ice content deduced from the ice budget of the stratiform region of a tropical cloud cluster. *J. Atmos. Sci.*, **41,** 1717–1725.

Curry, J. A., and E. E. Ebert, 1992: Annual cycle of radiation fluxes over the Arctic Ocean: Sensitivity to cloud optical properties. *J. Climate,* **5,** 1267–1280.

——, C. D. Ardeel, and L. Tian, 1990: Liquid water content and precipitation characteristics of stratiform clouds as inferred from satellite microwave measurements. *J. Geophys. Res.*, **95,** 16 659–16 671.

Deardorff, J. W., 1980: Cloud-top entrainment instability. *J. Atmos. Sci.*, **37,** 131–147.

Del Genio, A. D., 1993: Convective and large-scale cloud processes in GCMs. *Energy and Water Cycles in the Climate System,* E. Raschke and D. Jacob, Eds., NATO ASI Series, Vol. I5, Springer-Verlag, 95–121.

——, and M.-S. Yao, 1993: Efficient cumulus parameterization for long-term climate studies: The GISS scheme. *The Representation of Cumulus Convection in Numerical Models, Meteor. Monogr.,* No. 46, Amer. Meteor. Soc., 181–184.

——, W. Kovari, and M.-S. Yao, 1994: Climatic implications of the seasonal variation of upper troposphere water vapor. *Geophys. Res. Lett.*, **21,** 2701–2704.

Feigelson, E. M., 1978: Preliminary radiation model of a cloudy atmosphere. Part I: Structure of clouds and solar radiation. *Beitr. Phys. Atmos.*, **51,** 203–229.

Fowler, L. D., D. A. Randall, and S. A. Rutledge, 1995: Liquid and ice cloud microphysics in the CSU general circulation model. Part 1: Model description and simulated microphysical processes. *J. Climate,* in press.

Fu, R., A. D. Del Genio, and W. B. Rossow, 1990: Behavior of deep convective clouds in the tropical Pacific deduced from ISCCP radiances. *J. Climate,* **3,** 1129–1152.

——, ——, ——, and W. T. Liu, 1992: Cirrus cloud thermostat for tropical sea surface temperatures tested using satellite data. *Nature,* **358,** 394–397.

Gamache, J. F., and R. A. Houze Jr., 1983: Water budget of a mesoscale convective system in the Tropics. *J. Atmos. Sci.*, **40,** 1835–1850.

Griffith, K. T., S. K. Cox, and R. G. Knollenberg, 1980: Infrared radiative properties of tropical cirrus clouds inferred from aircraft measurements. *J. Atmos. Sci.*, **37,** 1077–1087.

Han, Q., W. B. Rossow, and A. A. Lacis, 1994: Near-global survey of effective cloud droplet radii in liquid water clouds using ISCCP data. *J. Climate,* **7,** 465–497.

Hansen, J. E., and L. D. Travis, 1974: Light scattering in planetary atmospheres. *Space Sci. Rev.*, **16,** 527–610.

——, G. Russell, D. Rind, P. Stone, A. Lacis, S. Lebedeff, R. Ruedy, and L. Travis, 1983: Efficient three-dimensional global models for climate studies: Models I and II. *Mon. Wea. Rev.*, **111,** 609–662.

Hanson, H. P., 1991: Cloud albedo control by cloud-top entrainment. *Tellus,* **43A,** 37–48.

Hartke, G. J., and D. Rind, 1995: An improved boundary layer model for the GISS GCM. *J. Climate,* submitted.

Heymsfield, A. J., and L. J. Donner, 1990: A scheme for parameterizing ice-cloud water content in general circulation models. *J. Atmos. Sci.*, **47,** 1865–1877.

Hobbs, P. V., and A. L. Rangno, 1985: Ice particle concentrations in clouds. *J. Atmos. Sci.*, **42,** 2523–2549.

Klein, S. A., and D. L. Hartmann, 1993: The seasonal cycle of low stratiform clouds. *J. Climate,* **6,** 1587–1606.

Kousky, V. E., and A. Leetmaa, 1989: The 1986–87 Pacific warm episode: Evolution of oceanic and atmospheric anomaly fields. *J. Climate,* **2,** 254–267.

Kuo, H., and W. H. Schubert, 1988: Stability of cloud-topped boundary layers. *Quart. J. Roy. Meteor. Soc.*, **114,** 887–916.

LeTreut, H., and Z.-X. Li, 1991: Sensitivity of an atmospheric general circulation model to prescribed SST changes: Feedback effects associated with the simulation of cloud optical properties. *Climate Dyn.*, **5,** 175–187.

Li, Z.-X., and H. LeTreut, 1992: Cloud-radiation feedbacks in a general circulation model and their dependence on cloud modelling assumptions. *Climate Dyn.*, **7,** 133–139.

Liao, X., W. B. Rossow, and D. Rind, 1995a: Comparison between SAGE II and ISCCP high-level clouds. Part I: Global and zonal mean cloud amounts. *J. Geophys. Res.*, **100,** 1121–1135.

——, D. Rind, and W. B. Rossow, 1995b: Comparison between SAGE II and ISCCP high-level clouds. Part II: Locating cloud tops. *J. Geophys. Res.*, **100,** 1137–1147.

Lin, B., and W. B. Rossow, 1994: Observations of cloud liquid water path over oceans: Optical and microwave remote sensing methods. *J. Geophys. Res.*, **99,** 20 909–20 927.

MacVean, M. K., 1993: A numerical investigation of the criterion for cloud-top entrainment instability. *J. Atmos. Sci.*, **50,** 2481–2495.

——, and P. J. Mason, 1990: Cloud-top entrainment instability through small-scale mixing and its parameterization in numerical models. *J. Atmos. Sci.*, **47,** 1012–1030.

Mason, B. J., 1971: *The Physics of Clouds.* Oxford University Press, 671 pp.

Miller, R. L., and A. D. Del Genio, 1994: Tropical cloud feedbacks and decadal variability of climate. *J. Climate,* **7,** 1388–1402.

Minnis, P., K.-N. Liou, and Y. Takano, 1993: Inference of cirrus cloud properties using satellite-observed visible and infrared radiances. Part I: Parameterization of radiance fields. *J. Atmos. Sci.*, **50,** 1279–1304.

Mitchell, J. F. B., C. A. Senior, and W. J. Ingram, 1989: CO_2 and climate: A missing feedback? *Nature,* **341,** 132–134.

Mokhov, I. I., and M. E. Schlesinger, 1994: Analysis of global cloudiness 2. Comparison of ground-based and satellite-based cloud climatologies. *J. Geophys. Res.*, **99,** 17 045–17 065.

Nakajima, T., M. D. King, J. D. Spinhirne, and L. F. Radke, 1991: Determination of the optical thickness and effective particle radius of clouds from reflected solar radiation measurements. Part II: Marine stratocumulus observations. *J. Atmos. Sci.*, **48,** 728–750.

Oort, A. H., 1983: Global Atmospheric Circulation Statistics, 1958–1973. NOAA Prof. Paper 14, NOAA Geophysical Fluid Dynamics Laboratory, U.S. Dept. of Commerce, 180 pp.

Platt, C. M. R., 1989: The role of cloud microphysics in high-cloud feedback effects on climate change. *Nature,* **341,** 428–429.

Prather, M. J., 1986: Numerical advection by conservation of second order moments. *J. Geophys. Res.*, **91,** 6671–6680.

Ramanathan, V., and W. Collins, 1991: Thermodynamic regulation of ocean warming by cirrus clouds deduced from observations of the 1987 El Niño. *Nature,* **351,** 27–32.

Randall, D. A., 1980: Conditional instability of the first kind upside-down. *J. Atmos. Sci.*, **37,** 125–130.

Roeckner, E., U. Schlese, J. Biercamp, and P. Loewe, 1987: Cloud optical depth feedbacks and climate modelling. *Nature,* **329,** 138–140.

Rosenzweig, C., and F. Abramopoulos, 1995: Land surface model development for the GISS GCM. *J. Climate,* submitted.

Rossow, W. B., and R. A. Schiffer, 1991: ISCCP cloud data products. *Bull. Amer. Meteor. Soc.*, **72,** 2–20.

Sassen, K., and G. C. Dodd, 1989: Haze particle nucleation simulations in cirrus clouds and applications for numerical and lidar studies. *J. Atmos. Sci.*, **46,** 3005–3014.

Schlesinger, M. E., and J.-H. Oh, 1993: A cloud-evaporation parameterization for general circulation models. *Mon. Wea. Rev.*, **121,** 1239–1248.

Senior, C. A., and J. F. B. Mitchell, 1993: Carbon dioxide and climate: The impact of cloud parameterization. *J. Climate,* **6,** 393–418.

Siems, S. T., C. S. Bretherton, M. B. Baker, S. Shy, and R. E. Briedenthal, 1990: Buoyancy reversal and cloud-top entrainment instability. *Quart. J. Roy. Meteor. Soc.*, **116,** 705–739.

Slingo, A., S. Nicholls, and J. Schmetz, 1982: Aircraft observations of marine stratocumulus during JASIN. *Quart. J. Roy. Meteor. Soc.*, **108,** 833–856.

Smith, R. N. B., 1990: A scheme for predicting layer clouds and their water content in a general circulation model. *Quart. J. Roy. Meteor. Soc.*, **116,** 435–460.

Soden, B. J., and F. P. Bretherton, 1993: Upper tropospheric relative humidity from the GOES 6.7 μm channel: Method and climatology for July 1987. *J. Geophys. Res.*, **98,** 16 669–16 688.

Starr, D. O'C., and D. P. Wylie, 1990: The 27–28 October 1986 FIRE cirrus case study: Meteorology and clouds. *Mon. Wea. Rev.*, **118,** 2259–2287.

Stephens, G. L., G. W. Paltridge, and C. M. R. Platt, 1978: Radiation profiles in extended water clouds. Part III: Observations. *J. Atmos. Sci.*, **35,** 2133–2141.

Sundqvist, H., 1978: A parameterization scheme for non-convective condensation including prediction of cloud water content. *Quart. J. Roy. Meteor. Soc.*, **104,** 677–690.

——, E. Berge, and J. E. Kristjansson, 1989: Condensation and cloud parameterization studies with a mesoscale numerical weather prediction model. *Mon. Wea. Rev.*, **117,** 1641–1657.

Tiedtke, M., 1993: Representation of clouds in large-scale models. *Mon. Wea. Rev.*, **121,** 3040–3061.

Tselioudis, G., W. B. Rossow, and D. Rind, 1992: Global patterns of cloud optical thickness variation with temperature. *J. Climate,* **5,** 1484–1495.

Twomey, S., 1977: *Atmospheric Aerosols.* Elsevier, 302 pp.

Walcek, C. J., 1994: Cloud cover and its relationship to relative humidity during a springtime midlatitude cyclone. *Mon. Wea. Rev.*, **122,** 1021–1035.

Warren, S. G., C. J. Hahn, J. London, R. M. Chervin, and R. L. Jenne, 1986: Global distribution of total cloud cover and cloud type amounts over land. NCAR/TN-273 + STR/DOE Tech. Rep. ER/60085-H1, 29 pp. + 200 maps.

——, ——, ——, ——, and ——, 1988: Global distribution of total cloud cover and cloud type amounts over ocean. NCAR/TN-317 + STR/DOE Tech. Rep. ER-0406, 42 pp. + 170 maps.

Wielicki, B. A., J. T. Suttles, A. J. Heymsfield, R. M. Welch, J. D. Spinhirne, M.-L. C. Wu, D. O'C. Starr, L. Parker, and R. F. Arduini, 1990: The 27–28 October 1986 FIRE IFO cirrus case study: Comparison of radiative transfer theory with observations by satellite and aircraft. *Mon. Wea. Rev.*, **118,** 2356–2376.

Xu, K.-M., and S. K. Krueger, 1991: Evaluation of cloudiness parameterizations using a cumulus ensemble model. *Mon. Wea. Rev.*, **119,** 342–367.

Ye, B., A. D. Del Genio, and K. K.-W. Lo, 1995: CAPE variations in the current climate and in a climate change. *J. Climate,* submitted.